Superconductivity from piezoelectric interactions in Weyl semimetals

Rodrigo G. Pereira,[1,2] Francesco Buccheri,[2] Alessandro De Martino,[3] and Reinhold Egger[2]

[1]*International Institute of Physics and Departamento de Física Teórica e Experimental, Universidade Federal do Rio Grande do Norte, Campus Universitario, Lagoa Nova, Natal-RN 59078-970, Brazil*
[2]*Institut für Theoretische Physik, Heinrich-Heine-Universität, D-40225 Düsseldorf, Germany,*
[3]*Department of Mathematics, City, University of London, EC1V 0HB London, UK*

We present an analytical low-energy theory of piezoelectric electron-phonon interactions in undoped Weyl semimetals, taking into account also Coulomb interactions. We show that piezoelectric interactions generate a long-range attractive potential between Weyl fermions. This potential comes with a characteristic angular anisotropy. From the one-loop renormalization group approach and a mean-field analysis, we predict that superconducting phases with either conventional *s*-wave singlet pairing or nodal-line triplet pairing could be realized for sufficiently strong piezoelectric coupling. For small couplings, we show that the quasiparticle decay rate exhibits a linear temperature dependence where the prefactor vanishes only in a logarithmic manner as the quasiparticle energy approaches the Weyl point. For practical estimates, we consider the Weyl semimetal TaAs.

I. INTRODUCTION

The physics of three-dimensional (3D) Weyl semimetals (WSMs) is presently attracting a lot of interest. For several different candidate materials, experiments have recently revealed WSM signatures in various observables [1–3]. Within band theory, WSMs have an even number of touching points (the so-called Weyl nodes) in the Brillouin zone. Near those special points, low-energy quasiparticles have a linear spectrum and represent Weyl fermions [4–9]. The Weyl character of low-energy fermions implies the existence of a chiral anomaly which in turn produces characteristic signatures in experimentally accessible observables such as the magnetoconductivity [8]. The remarkable transport features of WSMs may also lead to useful practical applications [10,11].

We here study the theory of electron-phonon (*e*-ph) interactions in WSMs. Apart from the case of optical phonons [12–17], the exploration of *e*-ph coupling effects in WSMs has not received much attention by theorists so far. However, it has been pointed out that in the static (frozen phonon) limit, strain engineering can be used to induce pseudo-scalar and pseudovector potentials that couple to Weyl fermions [18–24]. We here focus on low-energy long-wavelength acoustic phonons with linear dispersion, schematically written as $\Omega(\mathbf{q}) = c_{\rm ph}|\mathbf{q}|$ with sound velocity $c_{\rm ph}$. The linear dispersion of phonons as well as Weyl fermions suggests the existence of a scale-invariant effective action that may allow for nontrivial fixed points under the renormalization group (RG). We shall assume below that all relevant phonon momenta are well below the momentum separation b between a time-reversed pair of Weyl nodes, $|\mathbf{q}| \ll b$, such that phonons cannot scatter electrons between Weyl points at low temperatures. However, at elevated temperatures, $T \gtrsim c_{\rm ph}b/k_B$, this assumption breaks down and additional processes not considered in this work could take place.

For insulators or semiconductors, the most important couplings between electrons and acoustic phonons generally originate from either the deformation potential or the piezoelectric interaction [25–27]. While the former is a short-range interaction, the latter represents an anisotropic long-range interaction that only exists for inversion-symmetry-breaking crystals. The so-called direct piezoelectric effect refers to the appearance of an electric polarization when a material is subjected to static stress. On the other hand, in a metal, free charge carriers will screen the electric fields produced by local dipole moments, thereby preventing any macroscopic polarization. Nonetheless, it is still possible to speak of piezoelectricity in metals by measuring the bulk electric current in response to a time-dependent strain [28,29]. Electric currents in response to strain have been discussed in the context of WSMs in Ref. [30]. Below we will employ piezoelectric coupling expressions derived within the phenomenological theory of electronic insulators [31]. The main assumptions behind this approach are that the electric field produced by phonons is approximately longitudinal, and that there are no free charge carriers responsible for screening. In that case, $\nabla \cdot \mathbf{D} = 0$ can be assumed for the electric displacement field $\mathbf{D}$. A microscopic derivation of the piezoelectric coupling [32] gives further support to this phenomenological theory. The microscopic approach directly applies to insulators, where one can neglect the frequency dependence of the permittivity at frequencies well below the energy gap.

In *undoped* WSMs, the Fermi level is aligned with a Weyl point. Albeit the spectrum is gapless, screening is absent since the density of states vanishes at the Weyl point even when weak disorder is taken into account [33]. In fact, electron-electron (*e*-*e*) interactions are marginally irrelevant in 3D WSMs, such that the dielectric function picks up only logarithmic corrections at low energy scales [34–38]. However, when computing finite-temperature observables, it may be necessary to include the dynamic screening effects represented by these logarithmic corrections, as we will discuss in Sec. V in more detail.

We thus conclude that the piezoelectric coupling in undoped WSMs can be obtained along the lines of Refs. [27,31,32], see Eq. (21) below. If piezoelectric couplings are finite, then we find that they dominate over all other types of e-ph couplings which represent RG-irrelevant short-range interactions. Since many WSMs discovered so far belong to polar crystal symmetry classes, e.g., the ditetragonal-pyramidal 4mm class for TaAs, piezoelectric couplings are expected to play an important role for a wide class of WSM materials. Our general results will below be illustrated for the concrete case of TaAs, which also represents one of the experimentally most intensely studied WSMs [39–48]. For related ab $initio$ results, see Refs. [49,50].

In this paper, we present an analytical theory capturing the generic low-energy physics of undoped 3D WSMs taking into account the piezoelectric e-ph interaction. We also include e-e interactions even though they represent marginally irrelevant perturbations in WSMs. Nonetheless, their interplay with the piezoelectric coupling may lead to an instability in the RG flow [51] which drives the WSM into a Weyl superconductor [9,52–58] phase. For a similar but different study of e-e and e-ph interactions in the context of 2D Dirac fermions in graphene layers, see Ref. [59]. The main limitations of our theory come from the neglect of disorder and from the often rather complex band structure of real WSM materials. Moreover, we confine ourselves to $bulk$ properties only, leaving studies of surface state properties to future research.

The structure of the remainder of this paper is as follows. In Sec. II, we explain the model used in our study, derive the piezoelectric coupling Hamiltonian, and introduce a local field theory capturing both e-e and e-ph interactions. We use this field theory to derive the effective interaction potential between two Weyl fermions and show that the phonon-mediated attractive contribution has a characteristic angular anisotropy. In Sec. II E, we provide parameter estimates for the example of TaAs. In Sec. III, we then derive and discuss the RG equations found from a one-loop analysis. We continue in Sec. IV by investigating the stability of different superconducting phases by an analytical mean-field analysis. In addition, in Sec. V, we address the temperature and momentum dependence of the quasiparticle decay rate for small piezoelectric couplings where no interaction-induced instabilities are expected. Finally, we offer our conclusions in Sec. VI. Technical details can be found in the Appendix. We put $\hbar = k_B = 1$ throughout.

II. PIEZOELECTRIC INTERACTIONS IN WEYL SEMIMETALS

In this section, we describe the model used in this work and derive the piezoelectric coupling between electrons and acoustic phonons in undoped WSMs. We first briefly summarize the electronic Weyl Hamiltonian in Sec. II A, and then discuss a general acoustic phonon model in Sec. II B. We proceed in Sec. II C with a derivation of the piezoelectric coupling Hamiltonian. Next, in Sec. II D, we introduce a local field theory approach in order to capture both Coulomb interactions and piezoelectric interactions on equal footing. We also derive the attractive phonon-mediated potential and show that it exhibits a pronounced angular anisotropy.

A. Weyl Hamiltonian

In the absence of e-e and e-ph interactions, fermionic quasiparticles near a given Weyl node are described by the Weyl Hamiltonian [4–8],

$$H_0 = \sum_{\mathbf{p}} \psi^\dagger(\mathbf{p})[v_\perp \mathbf{p}_\perp \cdot \boldsymbol{\sigma}_\perp + v_3 p_3 \sigma_3]\psi(\mathbf{p}), \quad (1)$$

where the momentum $\mathbf{p} = (\mathbf{p}_\perp, p_3)$ is measured with respect to the Weyl node, $\psi = (\psi_\uparrow, \psi_\downarrow)^t$ is a spinor field operator, and the Pauli matrices $\boldsymbol{\sigma}_\perp = (\sigma_1, \sigma_2)$ and σ_3 (with identity σ_0) act in spin space. In Eq. (1) we consider anisotropic Fermi velocities, $v_3 \neq v_\perp$. In fact, such anisotropies can be generated by the piezoelectric interaction in crystals with tetragonal symmetry, see Sec. III A 4 below. However, for simplicity, we will often specialize to the isotropic case with

$$v_\perp = v_3 = v. \quad (2)$$

Throughout we assume that the chemical potential is located exactly at the Weyl node.

WSMs have an even number $2N$ of Weyl nodes in the Brillouin zone. In particular, time-reversal invariant WSMs with at least four Weyl nodes generically appear as intermediate phases between the trivial and the topological insulator phases of noncentrosymmetric semiconductors, where—depending on the space group of the crystal—all $2N$ Weyl nodes could be located at the Fermi level [60,61]. For a continuum model that produces four Weyl nodes by breaking the reflection symmetry of a Dirac semimetal, see Ref. [6].

Below we employ the fermionic Matsubara Green's function (GF) [25,62] for Weyl fermions near a given node,

$$G_{\sigma\sigma'}(x - x') = -\langle T_\tau \psi_\sigma(x)\psi_{\sigma'}^\dagger(x')\rangle, \quad (3)$$

where T_τ denotes imaginary time (τ) ordering, the spin index is $\sigma = \uparrow, \downarrow$, and we use the four-vector notation $x = (\tau, \mathbf{r})$. Taking the Fourier transform, with four-momentum $p = (i\omega, \mathbf{p})$, the GF has the spin matrix form

$$\mathbb{G}(x) = \frac{1}{\beta V} \sum_p e^{-i\omega\tau + i\mathbf{p}\cdot\mathbf{r}} \mathbb{G}(p), \quad (4)$$

where ω denotes fermionic Matsubara frequencies, the volume is V, and $\beta = 1/T$. Equation (1) yields the GF matrix

$$\mathbb{G}(p) = \frac{i\omega\sigma_0 + v_\perp \mathbf{p}_\perp \cdot \boldsymbol{\sigma}_\perp + v_3 p_3 \sigma_3}{(i\omega)^2 - E^2(\mathbf{p})}, \quad (5)$$

which has poles at $i\omega = \pm E(\mathbf{p})$ with

$$E(\mathbf{p}) = \sqrt{v_\perp^2 \mathbf{p}_\perp^2 + v_3^2 p_3^2}. \quad (6)$$

Such a gapless dispersion relation is characteristic for 3D Weyl fermions. For the isotropic case (2), this yields the familiar massless Weyl fermion dispersion with $E(\mathbf{p}) = v|\mathbf{p}|$. Unless noted otherwise, we consider the thermodynamic limit with $T = 0$, where all discrete sums such as those appearing in Eq. (4) are replaced by integrals. This step also implies that we investigate only bulk physics.

It will sometimes be advantageous to work in the band basis where $\mathbb{G}(p)$ is diagonal. Labeling these bands by $\mu = \pm$

and using Eq. (6), we find

$$G_{\mu\mu'}(p) = \frac{\delta_{\mu\mu'}}{i\omega - \mu E(\mathbf{p})} \equiv \delta_{\mu\mu'} G_\mu(p). \quad (7)$$

The mode expansion for the fermion field then reads

$$\psi_\sigma(\mathbf{r}) = \frac{1}{\sqrt{V}} \sum_{\mathbf{p}} \mathcal{U}_{\sigma\mu}(\mathbf{p})\psi_{\mathbf{p},\mu} e^{i\mathbf{p}\cdot\mathbf{r}}, \quad (8)$$

where $\mathcal{U}(\mathbf{p})$ is the unitary matrix that diagonalizes the single-particle Hamiltonian in Eq. (1). Note that $\mathcal{U} = \mathcal{U}(\hat{\mathbf{p}})$ is a function of the angles defined by the unit vector $\hat{\mathbf{p}} = \mathbf{p}/|\mathbf{p}|$ in momentum space. The Fourier transform of the electron density operator, $\rho_e(\mathbf{r}) = \psi^\dagger\psi$, is then given by

$$\rho_e(\mathbf{q}) = \sum_{\mathbf{p},\mu,\mu'} [\mathcal{U}^\dagger(\mathbf{p})\mathcal{U}(\mathbf{p}+\mathbf{q})]_{\mu\mu'}\psi^\dagger_{\mathbf{p}\mu}\psi_{\mathbf{p}+\mathbf{q},\mu'}. \quad (9)$$

Allowing for contributions from all $2N$ Weyl nodes in the Brillouin zone (indexed by h), we have $\rho_e(\mathbf{r}) = \sum_h \psi^\dagger_h \psi_h$.

B. Phonons

We here focus on acoustic phonons at long wave lengths. The physics is then described by the lattice displacement field $\mathbf{u}(\mathbf{r})$. With the linearized strain tensor,

$$u_{jk} = \tfrac{1}{2}(\partial_j u_k + \partial_k u_j), \quad (10)$$

and the fourth-order stiffness tensor C_{ijkl}, the Euclidean action is given by [25,63]

$$S_{\text{ph}} = \int d^4x \left[\frac{\rho_0}{2}(\partial_\tau \mathbf{u})^2 + \frac{1}{2}\sum_{ijkl} C_{ijkl} u_{ij} u_{kl} \right], \quad (11)$$

where ρ_0 is the mass density and $d^4x = d\tau d^3\mathbf{r}$. Our main interest in this work is in describing possible electronic instabilities of WSMs due to piezoelectric interactions, and we will therefore not study a specific phonon model. We assume instead that all three ($J = 1, 2, 3$) acoustic phonon modes have a linear dispersion,

$$\Omega_J(\mathbf{q}) = c_J(\hat{\mathbf{q}})\,|\mathbf{q}|, \quad (12)$$

where the respective sound velocity, $c_J(\hat{\mathbf{q}})$, could depend on the angular direction $\hat{\mathbf{q}} = \mathbf{q}/|\mathbf{q}|$. Using bosonic annihilation operators, $a_J(\mathbf{q})$, the standard mode expansion of the lattice displacement field is given by [25]

$$\mathbf{u}(\mathbf{r}) = \sum_{J=1}^3 \sum_{\mathbf{q}} \frac{\boldsymbol{\epsilon}^J(\mathbf{q}) e^{i\mathbf{q}\cdot\mathbf{r}}}{\sqrt{2\rho_0 V \Omega_J(\mathbf{q})}} a_J(\mathbf{q}) + \text{H.c.}, \quad (13)$$

where the $\boldsymbol{\epsilon}^J(\mathbf{q})$ are polarization unit vectors.

Next we define the phonon propagator [62],

$$D_{jk}(x - x') = -\langle T_\tau u_j(x)u_k(x')\rangle. \quad (14)$$

Taking the Fourier transform and using $q = (i\omega, \mathbf{q})$ with bosonic Matsubara frequencies ω, we obtain from Eqs. (12) and (14) the result

$$D_{jk}(q) = \frac{1}{\rho_0} \sum_J \frac{\epsilon^J_j(\mathbf{q})\epsilon^J_k(-\mathbf{q})}{(i\omega)^2 - \Omega_J^2(\mathbf{q})} = D_{kj}(-q). \quad (15)$$

For an isotropic continuum, we may identify $J = 1$ with the longitudinal mode and $J = 2, 3$ with the transverse modes, where $c_1 = c_l$ and $c_{2,3} = c_t$ denote the longitudinal and transverse sound velocities, respectively. We will often make the simplifying assumption

$$c_t = c_l = c_{\text{ph}}, \quad c_{\text{ph}} \ll v, \quad (16)$$

on top of the isotropic Fermi velocity condition (2). These assumptions do not affect scaling properties in an essential way. Moreover, relaxing those approximations does not pose conceptual problems and could allow one to take into account *ab initio* results, see, e.g., Refs. [50,64].

C. Piezoelectric interaction

A microscopic derivation of the *e*-ph interaction in insulators encounters short-range as well as long-range interactions [27,32]. The long-range contributions can be organized in terms of a multipole expansion of the electron-ion interaction potential. The first term in this expansion is a dipolar contribution which must vanish due to the acoustic sum rule. The next terms are quadrupolar contributions which account for piezoelectric couplings and vanish for centrosymmetric materials, but not when inversion symmetry is broken. A phenomenological derivation [26,31] starts from the constitutive relation for the electric displacement,

$$D_i = \sum_{jk} e_{ijk} u_{jk} + \sum_j \varepsilon_{ij} E_j, \quad (17)$$

where $\mathbf{E}$ is the external electric field, e_{ijk} the piezoelectric tensor, and ε_{ij} the permittivity tensor [25]. A nonvanishing piezoelectric tensor arises if strain can induce $\mathbf{D} \neq 0$ even for $\mathbf{E} = 0$. The relation $e_{ijk} = (\partial D_i/\partial u_{jk})_E$ and the symmetry of the strain tensor, $u_{jk} = u_{kj}$, imply that the piezoelectric tensor is symmetric in the last two indices, $e_{ijk} = e_{ikj}$.

In the absence of free charges, from Eq. (17) we have

$$\nabla \cdot \mathbf{D} = 0 = \sum_{ijk} e_{ijk}\partial_i u_{jk} + \sum_{ij} \varepsilon_{ij}\partial_i E_j. \quad (18)$$

Taking the Fourier transform gives

$$\sum_{ij} \varepsilon_{ij} q_i E_j(\mathbf{q}) = -i \sum_{ijk} e_{ijk} q_i q_j u_k(\mathbf{q}). \quad (19)$$

Since the electric field is effectively longitudinal [31], we can write $\mathbf{E}(\mathbf{q}) \simeq -i\mathbf{q}\Phi(\mathbf{q})$ with the scalar potential

$$\Phi(\mathbf{q}) = \frac{1}{\varepsilon\mathbf{q}^2} \sum_{ijk} e_{ijk} q_i q_j u_k(\mathbf{q}). \quad (20)$$

For notational simplicity, we assume an isotropic permittivity tensor, $\varepsilon_{ij} = \varepsilon\delta_{ij}$.

The scalar potential (20) now couples to the electronic charge density, cf. Eq. (9), resulting in the piezoelectric interaction Hamiltonian

$$H_{\text{pz}} = \frac{e}{\varepsilon V} \sum_{ijk} \sum_{\mathbf{q}\neq 0} e_{ijk} \frac{q_i q_j}{\mathbf{q}^2} u_k(\mathbf{q})\rho_e(-\mathbf{q}). \quad (21)$$

We emphasize that the coupling strength in Eq. (21) depends on the direction of the unit vector $\hat{\mathbf{q}}$, where the $\mathbf{q} = 0$ mode is omitted to ensure overall electric neutrality. From dimensional

analysis, H_{pz} is marginal under RG transformations, and second-order perturbation theory implies a linear-in-T dependence of the quasiparticle decay rate, see Sec. V for details. At low T, the piezoelectric interaction will therefore dominate over RG-irrelevant short-range contributions, e.g., from the deformation potential. We find that the latter terms generically cause a quasiparticle decay rate scaling as $\sim T^3$. In fact, for insulators and semiconductors, the piezoelectric interaction is known to dominate small-q scattering if it is allowed by crystal symmetries [26]. We emphasize that the piezoelectric interaction is marginal only in three spatial dimensions. In 2D systems, the corresponding operator is relevant instead. In practice, such interactions are then screened above a length scale defined by the bare coupling constant.

Finally, in view of the symmetry property $e_{ijk} = e_{ikj}$, it is customary to express the piezoelectric tensor in Voigt notation [31],

$$e_{ijk} = e_{i(jk)} \mapsto e_{im}, \quad m = 1, \ldots, 6, \quad (22)$$

where matrix elements with $(11) \mapsto 1$, $(22) \mapsto 2$, and $(33) \mapsto 3$ correspond to tension or compression, and those with $(23) = (32) \mapsto 4$, $(13) = (31) \mapsto 5$, and $(12) = (21) \mapsto 6$ describe shear. Depending on the crystal symmetry, the various components in Eq. (22) may be related to one another or they could vanish identically, see Ref. [65] for useful tables. For instance, for TaAs with space group $I4_1md$, No. 109, one finds only three independent components, namely e_{15}, e_{31}, and e_{33}. Their respective values have been computed by *ab initio* methods [50].

D. Electron-electron interactions

As we show below, the piezoelectric interaction (21) generates a long-range *e-e* interaction that is attractive in the low-frequency limit where retardation effects can be neglected. This phonon-mediated potential has a characteristic angular anisotropy and competes with the repulsive Coulomb interaction in undoped WSMs. We therefore also include Coulomb interactions from now on.

To that end, we express the Euclidean action of the system in local form by introducing a scalar bosonic Hubbard-Stratonovich field $\varphi(x)$, see Refs. [37,38]. Loosely speaking, the field φ describes photon modes mediating Coulomb interactions. It couples to the sources of the electric field, which include both the conduction electron density and the effective charge density generated by strain via the piezoelectric effect. With the phonon action S_{ph} in Eq. (11), we start from the total action

$$S = S_{\mathrm{ph}} + \int d^4x \left[Z_\psi^{-1} \psi^* \partial_\tau \psi - iv \psi^* (\nabla \cdot \boldsymbol{\sigma}) \psi \right.$$
$$\left. + \frac{Z_\varphi^{-1}}{2} (\nabla \varphi)^2 + i g_e \psi^* \psi \, \varphi + i g_{\mathrm{ph}} \sum_{jkl} e_{jkl} \partial_j \varphi \, u_{kl} \right].$$
$$(23)$$

The bare weight of the fermion (Coulomb) field is given by $Z_\psi = 1$ ($Z_\varphi = 1$). These factors could, however, change during the RG flow, see Sec. III. The partition function is
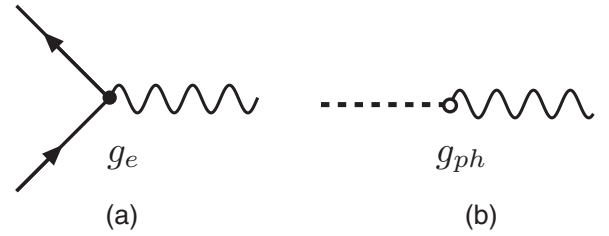

FIG. 1. Feynman diagrams for the vertices in Eq. (23), coupling the field φ (wiggly curve) to (a) electrons (solid line) and to (b) phonons (dashed). The Coulomb (piezoelectric) vertex $\sim g_e$ ($\sim g_{\mathrm{ph}}$) is shown as filled (open) circle.

thereby expressed as a functional integral over the fermionic Grassmann fields (ψ, ψ^*), the displacement field $\mathbf{u}$, and the field φ, i.e., $\mathcal{Z} = \int \mathcal{D}[\psi, \psi^*, \mathbf{u}, \varphi] e^{-S}$ [62]. For simplicity, we here assumed isotropic Fermi velocities, cf. Eq. (2), but we also discuss the general case in Sec. III. The action (23) contains two interaction vertices with couplings g_e and g_{ph}. Their diagrammatic representation is shown in Fig. 1.

In order to verify that Eq. (23) makes sense, let us now integrate out the bosonic field φ. With $\rho_e = \psi^* \psi$ and switching to Fourier space ($d^4q = d\omega d^3\mathbf{q}$), the interacting part of the action is then given by

$$S_{\mathrm{int}} = \int \frac{d^4q}{(2\pi)^4} \left[\frac{g_e^2}{2|\mathbf{q}|^2} \rho_e(q) \rho_e(-q) \right.$$
$$+ g_e g_{\mathrm{ph}} \sum_{ijk} e_{ijk} \frac{q_i q_j}{|\mathbf{q}|^2} u_k(q) \rho_e(-q)$$
$$\left. + \frac{g_{\mathrm{ph}}^2}{2} \sum_{ijk} \sum_{lmn} e_{ijk} e_{lmn} \frac{q_i q_j q_l q_m}{|\mathbf{q}|^2} u_k(q) u_n(-q) \right]. \quad (24)$$

The first term corresponds to the Coulomb *e-e* interaction on choosing $g_e^2 = e^2/\varepsilon$, while the second term reproduces the piezoelectric interaction (21) for $g_e g_{\mathrm{ph}} = e/\varepsilon$. The bare couplings are therefore given by

$$g_e = \frac{e}{\sqrt{\varepsilon}}, \quad g_{\mathrm{ph}} = \frac{1}{\sqrt{\varepsilon}}. \quad (25)$$

We emphasize that the charge e is associated only with the Coulomb vertex $\sim g_e$ in Fig. 1. In Eqs. (23) and (24), we have tacitly assumed that intra- and internode Coulomb interactions can be taken identical. Since the effects considered in our paper come from the long-range $1/r$ tail of the Coulomb potential, the couplings between long-wavelength density fluctuations ρ_h and $\rho_{h'}$ of electrons near the Weyl nodes h and h', respectively, are approximately described by the same potential. The last term in Eq. (24) describes the energy density associated with strain-induced electric fields. Being quadratic in the strain tensor, this contribution generates the so-called piezoelectric stiffening correction, see Ref. [65] for details. This modification of the phonon dispersion typically acts to increase sound velocities [16,65]. Since here our main interest is centered on electronic instabilities, we will simply assume that the phonon velocities $c_J(\hat{\mathbf{q}})$ in Eq. (12) already incorporate piezoelectric stiffening to all orders in g_{ph}.
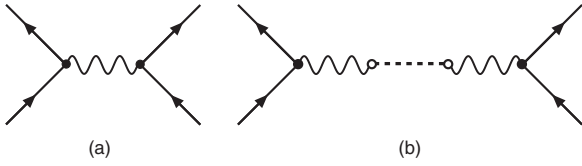
FIG. 2. Effective *e-e* interaction at tree level. (a) Repulsive Coulomb interaction. (b) Phonon-mediated *e-e* interaction, see Eq. (26).

Next we discuss the effective interaction potential between two Weyl fermions described by the above theory. The two diagrams determining the effective *e-e* interaction at tree level, i.e., to lowest nontrivial order in perturbation theory, are illustrated in Fig. 2. In particular, Fig. 2(b) defines a retarded *e-e* interaction potential, $V_{\rm ph}(q)$, mediated by the piezoelectric interaction, where $q = (i\omega, \mathbf{q})$ is the exchanged four-momentum. Using Eq. (23) and the phonon propagator in Eq. (15), we find

$$V_{\rm ph}(q) = \sum_J \frac{g_e^2 g_{\rm ph}^2 / \rho_0}{(i\omega)^2 - \Omega_J^2(\mathbf{q})} \sum_{ijk} \frac{\left| e_{ijk} q_i q_j \epsilon_k^J(\hat{\mathbf{q}}) \right|^2}{|\mathbf{q}|^4}. \quad (26)$$

Neglecting retardation effects by going to the static limit, $\omega \to 0$, the potential can be written as

$$V_{\rm ph}(\mathbf{q}) = -\frac{g_e^2 g_{\rm ph}^2}{\rho_0 \mathbf{q}^2} \gamma(\hat{\mathbf{q}}), \quad \gamma(\hat{\mathbf{q}}) = \sum_{J=1}^3 \gamma_J(\hat{\mathbf{q}}), \quad (27)$$

with the anisotropy functions

$$\gamma_J(\hat{\mathbf{q}}) = \frac{1}{c_J^2(\hat{\mathbf{q}}) |\mathbf{q}|^4} \left| \sum_{ijk} e_{ijk} q_i q_j \epsilon_k^J(\hat{\mathbf{q}}) \right|^2, \quad (28)$$

which describe the angular dependence of the phonon-mediated interaction. We emphasize that $\gamma(\hat{\mathbf{q}}) > 0$ for all directions $\hat{\mathbf{q}}$, and thus the interactions in Eq. (27) are always attractive. Combining Eq. (27) with the long-range Coulomb interaction in Fig. 2(a), we arrive at the total *e-e* interaction potential

$$V_{\rm tot}(\mathbf{q}) = \frac{g_e^2}{\mathbf{q}^2} \left[1 - \frac{g_{\rm ph}^2}{\rho_0} \gamma(\hat{\mathbf{q}}) \right]. \quad (29)$$

Let us now consider WSMs in the 4*mm* crystal class, which in particular includes TaAs, and also use the simplifications in Eqs. (2) and Eq. (16). In Voigt notation, see Sec. II C, we define the ratios of piezoelectric coefficients

$$A = \frac{e_{15}}{e_{33}}, \quad B = \frac{e_{31}}{e_{33}}. \quad (30)$$

The anisotropy function $\gamma = \gamma(\theta)$ now depends only on the polar angle θ of $\hat{\mathbf{q}}$. To evaluate Eq. (28), the polarization unit vectors are parametrized as

$$\boldsymbol{\epsilon}^1(\hat{\mathbf{q}}) = i\hat{\mathbf{q}}, \quad \boldsymbol{\epsilon}^2(\hat{\mathbf{q}}) = \frac{i\hat{\mathbf{z}} \times \hat{\mathbf{q}}}{|\hat{\mathbf{z}} \times \hat{\mathbf{q}}|}, \quad \boldsymbol{\epsilon}^3(\hat{\mathbf{q}}) = \hat{\mathbf{q}} \times \boldsymbol{\epsilon}^2(\hat{\mathbf{q}}), \quad (31)$$

leading to

$$\gamma_1(\theta) = \frac{e_{33}^2}{c_{\rm ph}^2} \cos^2 \theta [1 + (2A + B - 1) \sin^2 \theta]^2$$

$$\gamma_2(\theta) = 0 \quad (32)$$

$$\gamma_3(\theta) = \frac{e_{33}^2}{c_{\rm ph}^2} \sin^2 \theta [(B - 1) \cos^2 \theta + A \cos(2\theta)]^2.$$

The contribution from the $J = 2$ transverse mode, where the polarization is always perpendicular to $\hat{\mathbf{z}}$, vanishes identically. More generally, $\gamma_J(\theta) = 0$ whenever $\boldsymbol{\epsilon}^J \cdot \hat{\mathbf{z}} = 0$.

In the simplest approximation, one may just average over the directions $\hat{\mathbf{q}}$ in Eq. (27), see Refs. [25,31]. We write the angular-averaged total interaction potential as

$$\bar{V}_{\rm tot}(\mathbf{q}) = \frac{g_e^2(1 - \bar{\gamma})}{\mathbf{q}^2}. \quad (33)$$

For the 4*mm* crystal class, we find from Eq. (32)

$$\bar{\gamma} = \frac{g_{\rm ph}^2}{2\rho_0} \int_0^\pi d\theta \sin(\theta) \gamma(\theta) = \frac{w_\gamma}{\rho_0} \left(\frac{g_{\rm ph} e_{33}}{c_{\rm ph}} \right)^2, \quad (34)$$

with the coefficient

$$w_\gamma = \frac{1}{15} [10A^2 + 4A(B + 1) + 2B^2 + 3]. \quad (35)$$

Clearly, for $\bar{\gamma} > 1$, the averaged total interaction (33) is attractive. One thus expects a gapped superconducting phase with *s*-wave singlet pairing. However, as we show in Sec. IV, for $\bar{\gamma} < 1$, one may also encounter more exotic superconducting phases exhibiting, e.g., nodal-line triplet pairing.

E. Parameter estimates

To get concrete predictions from our theory, we need information about the piezoelectric coefficients [66–68], the permittivity ε, the mass density ρ_0, and the Fermi as well as the sound velocities. Since in TaAs the lattice parameters are $a_\perp \simeq 3.43$ Å and $a_3 \simeq 11.6$ Å, and the conventional unit cell contains 4 Ta and 4 As ions, the mass density is $\rho_0 \simeq 1.24 \times 10^4$ kg/m³. For simplicity, we here adopt the simplifying assumptions in Eqs. (2) and (16). For the Fermi velocity, we take $\hbar v \simeq 2$ eV Å [43], which corresponds to $v \simeq 3 \times 10^5$ m/s. The sound velocity is assumed to be given by $c_{\rm ph} \simeq 6 \times 10^3$ m/s, cf. the value quoted in Ref. [69] for TaN. For the piezoelectric tensor of TaAs [50], we use $e_{33} = -1.89$ Cm⁻² and the ratios in Eq. (30) are $A \simeq -2.62$ and $B \simeq -0.43$. This gives $w_\gamma \simeq 4.40$. Using the rough estimate $\varepsilon \approx 20\varepsilon_0$ [38], we obtain $\alpha_{\rm eff} \approx 0.24$ and $\bar{\gamma} \approx 0.20$. The latter is well below the critical value $\bar{\gamma} = 1$. However, the value of $\bar{\gamma}$ could in principle be higher in other materials which might have, for instance, larger piezoelectric coefficients or smaller permittivity.

Moreover, the approximation in Eq. (33) neglects the angular anisotropy of the effective interaction. A polar plot of $\gamma(\theta)$ based on our estimates for TaAs is shown in Fig. 3(a). The attractive interaction strength is maximal for $\theta = \pi/2$. This shape of $\gamma(\theta)$ is representative of the regime $|e_{15}| > |e_{33}| > |e_{31}|$, which is also realized for the paradigmatic piezoelectric insulator BaTiO₃ [66]. For TaAs, the total *e-e* interaction potential is repulsive in all directions. However, for higher
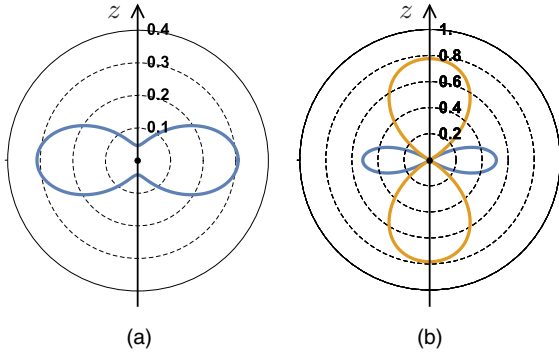
FIG. 3. (a) Polar plot of the anisotropy function $\gamma(\theta)$ in Eq. (27) for the case of TaAs, with $\gamma(\theta)$ multiplied by g_{ph}^2/ρ_0. We take $\varepsilon = 20\varepsilon_0$, where ε_0 is the free-space permittivity. The piezoelectric tensor values are taken from Ref. [50], where we get $\bar{\gamma} \simeq 0.20$ in Eq. (34). The blue color indicates that the phonon-mediated interaction is always attractive. (b) Effective anisotropy function of the total e-e interaction potential in Eq. (29), where we adjust e_{33} such that $\bar{\gamma} = 0.97$. Blue again indicates attraction while orange represents repulsion.

values of $\bar{\gamma}$ and depending on the relative strength of the Coulomb and the piezoelectric terms, there may be directions along which the total interaction potential becomes attractive even for $\bar{\gamma} < 1$. In this case, superconducting phases could be possible despite the effective repulsion in the s-wave channel. In Fig. 3(b), we show the angular dependence of the total e-e interaction potential (29) for $\bar{\gamma} = 0.97$. In this case, the total e-e interaction potential changes sign as a function of θ and becomes attractive for $\theta \simeq \pi/2$.

III. RG ANALYSIS

In this section, we turn to the derivation and solution of the one-loop RG equations. In an infinitesimal RG step, the flow parameter changes as $\ell \mapsto \ell + d\ell$, where $\Lambda(\ell) = e^{-\ell}\Lambda_0$ is the running high-energy bandwidth cutoff with bare value Λ_0. We obtain the RG equations by the standard momentum-shell integration approach, where in each RG step one integrates over all field modes appearing in the partition function with energies in the shell $\Lambda(\ell + d\ell) < E < \Lambda(\ell)$. The resulting contributions to the partition function are then taken into account by renormalization of the various couplings in the action, see Refs. [51,62].

We start from the observation that for the local field theory (23), perturbative expansions of physical observables involve only diagrams of the types shown in Fig. 4. In all these diagrams, fermion loop contributions always involve the Coulomb vertex $\sim g_e$. This fact can be rationalized by recalling that the piezoelectric interaction also arises from an expansion of the Coulomb potential, see Sec. II C. The vertex g_{ph} only appears in regular, perturbative corrections to the Coulomb propagator. At the one-loop level, perturbation theory in g_e generates the diagrams in Figs. 5(a), 5(b), and 5(c), which are precisely the diagrams that govern the one-loop renormalization of e-e interactions in the absence of phonons [38].

Within the static approximation with the angular-averaged interaction potential in Eq. (33), the piezoelectric interaction

is combined with the Coulomb e-e interaction and its effect amounts to replacing $g_e^2 \mapsto g_e^2(1 - \bar{\gamma})$. As a consequence, the essential physics of the system can be studied in terms of a single dimensionless coupling, namely the effective fine structure constant

$$\alpha_{\text{eff}} = \frac{g_e^2(1 - \bar{\gamma})}{4\pi v}. \tag{36}$$

Within this static approximation, the RG equation for α_{eff} at the one-loop level follows from the diagrams in Figs. 5(a), 5(b), and 5(c). The result is [38]

$$\frac{d\alpha_{\text{eff}}}{d\ell} = -\frac{2(N+1)}{3\pi}\alpha_{\text{eff}}^2. \tag{37}$$

Therefore, the system flows to strong coupling when the effective fine structure constant becomes negative. This happens for sufficiently strong piezoelectric coupling, in the regime $\bar{\gamma} > 1$.

The strong-coupling phase realized for $\bar{\gamma} > 1$ is expected to be an intrinsic superconductor since the attractive e-ph interaction then dominates over the repulsive Coulomb interaction. Previous work [6,53,56] has discussed intrinsic superconductivity in *doped* WSMs. The new element in our system
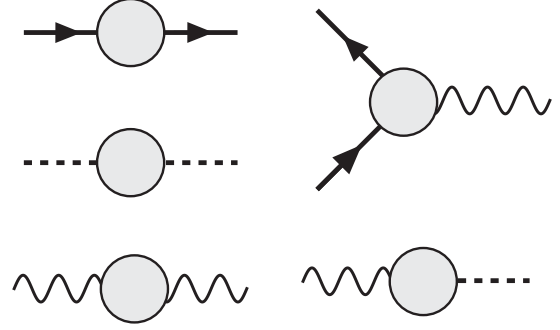

FIG. 4. Schematic form of the possible amplitudes generated by the local field theory in Eq. (23), where shaded regions represent dressed vertices in a perturbative expansion.
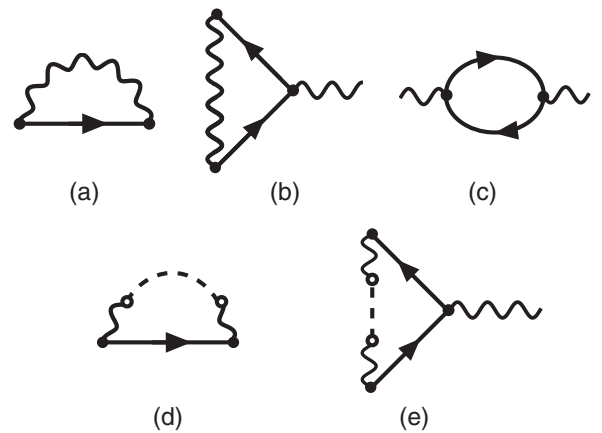

FIG. 5. Diagrams contributing to the one-loop RG equations. (a) Coulomb correction to the electronic self-energy. (b) Vertex correction due to Coulomb interaction. (c) Polarization bubble inserted in the Coulomb propagator. (d) Piezoelectric correction to the electronic self-energy. (e) Piezoelectric vertex correction.

is the long-range *e-e* interaction resulting from a combination of unscreened Coulomb and piezoelectric interactions. We recall that the standard BCS formula for the superconducting gap is given by $\Delta \sim e^{-1/\nu_F |\lambda|}$, where ν_F is the normal density of states at the Fermi level and λ denotes the strength of the short-range attractive interaction. For vanishing ν_F, intrinsic superconductivity is not possible unless the short-range interaction exceeds a critical coupling of the order of the electronic bandwidth, far beyond the perturbatively accessible regime. As we will see in Sec. IV, the long-range character of the piezoelectric interaction allows for the opening of a finite gap even for the undoped case with $\nu_F = 0$. In this case, the gap is a function of the dimensionless parameter $\alpha_{\text{eff}} < 0$. Eliminating the need for doping to realize superconductivity in WSMs is important because the density of states cannot be made very large if one wants to stay below the energy scale vb, where b is the momentum separation between two Weyl nodes. In fact, at high energies, nonlinearities will appear in the dispersion relation.

A. RG equations beyond the static approximation

We can use the RG approach to analyze how the piezoelectric interaction affects the running couplings in the effective action (23) beyond the static approximation, i.e., including retardation effects. After performing an infinitesimal RG transformation and rescaling $\psi \mapsto (1 + \delta Z_\psi / Z_\psi)^{1/2} \psi$ and $\varphi \mapsto (1 + \delta Z_\varphi / Z_\varphi)^{1/2} \varphi$ to absorb the field renormalizations, we obtain a correction to the effective action of the form

$$
\delta S = \int d^4 x \left[-iv \left(1 + \frac{\delta v}{v} + \frac{\delta Z_\psi}{Z_\psi} \right) \psi^* (\nabla \cdot \boldsymbol{\sigma}) \psi \right.
$$

$$
+ ig_e \left(1 + \frac{\delta g_e}{g_e} + \frac{\delta Z_\psi}{Z_\psi} + \frac{1}{2} \frac{\delta Z_\varphi}{Z_\varphi} \right) \psi^* \psi\, \varphi
$$

$$
\left. + ig_{\text{ph}} \left(1 + \frac{\delta g_{\text{ph}}}{g_{\text{ph}}} + \frac{1}{2} \frac{\delta Z_\varphi}{Z_\varphi} \right) \sum_{jkl} e_{jkl} \partial_j \varphi\, u_{kl} \right]. \quad (38)
$$

We can compute δg_e and δg_{ph} from the corresponding vertex corrections, whereas δZ_ψ and δv stem from the electron self-energy and δZ_φ from the polarization insertion in the Coulomb propagator. The corrections can then be absorbed as a renormalization of the parameters v, g_e, and g_{ph}.

At the one-loop level and at lowest order in g_{ph}, the contributions from the piezoelectric interaction are represented by the diagrams shown in Figs. 5(d) and 5(e). The latter are generated by taking into account the (nondivergent) correction to the Coulomb propagator at order g_{ph}^2. In the following we will now separately discuss each of the five diagrams in Fig. 5.

1. Coulomb correction to the electronic self-energy

The standard rainbow diagram in Fig. 5(a) describes the lowest-order correction to the electronic self-energy due to Coulomb interactions. A well-known consequence of this contribution is a renormalization of the Fermi velocities. Related effects have been predicted and experimentally observed for graphene [70]. The diagram in Fig. 5(a) yields the

self-energy

$$
\Sigma_{ee}(p) = -g_e^2 \int \frac{d^4 q}{(2\pi)^4} \frac{1}{\mathbf{q}^2} \mathbb{G}(p+q), \quad (39)
$$

with $p = (i\omega, \mathbf{p})$. We evaluate Eq. (39) in Appendix A, where we show that Σ_{ee} does not depend on the frequency ω and hence no field renormalization arises from this term, $\delta Z_\psi = 0$. Integrating out the modes of the field φ within the high-energy momentum shell and keeping only self-energy terms linear in the momentum $\mathbf{p}$, we arrive at the self-energy correction

$$
\delta \Sigma_{ee}(\mathbf{p}) = \frac{g_e^2}{8\pi^2} (\eta_\perp \mathbf{p}_\perp \cdot \boldsymbol{\sigma}_\perp + \eta_3 p_3 \sigma_3) d\ell, \quad (40)
$$

where the numbers $\eta_\perp$ and η_3 depend on the Fermi velocity ratio $v_3 / v_\perp$, cf. Appendix A. By comparing with Eq. (1), we see that Eq. (40) generates a correction to the Fermi velocities $v_\perp$ and v_3. For the isotropic case (2), we get $\eta_\perp = \eta_3 = 4/3$. In this case, we obtain

$$
\delta v = \frac{g_e^2}{6\pi^2} d\ell. \quad (41)
$$

By itself, this term makes the Fermi velocity increase under the RG flow.

2. Vertex correction due to Coulomb interaction

Next we turn to the diagram in Fig. 5(b), which provides a vertex correction due to the Coulomb interaction, corresponding to a charge renormalization [62]. However, this diagram actually gives no contribution at all. In fact, the instantaneous Coulomb interaction does not give rise to charge renormalization for Weyl (or Dirac) fermions at the one-loop level [71]. For the corresponding 2D graphene case, charge renormalization is absent also at the two-loop level [71].

3. Coulomb propagator: Polarization bubble

At the one-loop level, the self-energy of the field φ comes from the standard polarization bubble in Fig. 5(c). Following the analysis of Ref. [38], the self-energy correction can be absorbed by the field renormalization of φ,

$$
\delta Z_\varphi = -\frac{N g_e^2}{6\pi^2 v} Z_\varphi d\ell, \quad (42)
$$

where the presence of a fermion loop in the diagram implies that this correction is proportional to the number of Weyl nodes, $2N$. For simplicity, we have again assumed isotropic Fermi velocities, see Eq. (2).

4. Piezoelectric self-energy correction

Next we turn to the electronic self-energy $\Sigma_{ep}(i\omega, \mathbf{p})$ due to *e*-ph interactions, which to one-loop order comes from the diagram in Fig. 5(d). We evaluate this term in Appendix B, see Eq. (B2). A nonuniversal contribution arises for $\omega = \mathbf{p} = 0$ which can be absorbed by renormalization of the chemical potential. A similar contribution also comes from *e-e* interactions, see Appendix A, and we eventually require the renormalized chemical potential to be located at the Weyl node. As discussed in Appendix B, for 4*mm* crystal symmetry

and again using Eqs. (2) and (16), the self-energy correction after momentum-shell integration is given by

$$
\delta\Sigma_{ep}(p) = -\frac{1}{4\pi\rho_0}\left(\frac{g_e g_{\mathrm{ph}} e_{33}}{c_{\mathrm{ph}}}\right)^2 \frac{c_{\mathrm{ph}}}{v}
$$
$$
\times \left(\frac{i\omega C_0}{v}\sigma_0 + C_\perp \mathbf{p}_\perp \cdot \boldsymbol{\sigma}_\perp + C_3 p_3 \sigma_3\right) d\ell, \quad (43)
$$

with the numbers $C_0 \simeq 1.40$, $C_\perp \simeq 0.29$, and $C_3 \simeq 0.83$ for TaAs. The smallness of the factor $c_{\mathrm{ph}}/v \ll 1$, together with the fact that in practice we have $\bar{\gamma} \lesssim 1$ in Eq. (34), implies that contributions from Eq. (43) to RG equations are rather small.

In marked contrast to the Coulomb case, we now encounter in Eq. (43) a term $\Sigma_{ep} \sim \omega$ responsible for field renormalization,

$$
\delta Z_\psi = -\frac{C_0}{4\pi\rho_0 v}\frac{c_{\mathrm{ph}}}{v}\left(\frac{g_e g_{\mathrm{ph}} e_{33}}{c_{\mathrm{ph}}}\right)^2 Z_\psi d\ell, \quad (44)
$$

implying that the quasiparticle weight Z_ψ decreases under the RG flow.

The $\mathbf{p} \neq 0$ terms in Eq. (43) can be absorbed by renormalization of the Fermi velocities. In general, even for initially isotropic velocities, the fact that $C_\perp \neq C_3$ implies that piezoelectric couplings intrinsically generate anisotropic Fermi velocities. Because we have $c_{\mathrm{ph}}/v \ll 1$, however, this Fermi velocity renormalization is typically subleading against the dominant Coulomb term in Eq. (41). For simplicity, we here neglect the RG-generated anisotropy of the Fermi velocities and only focus on the mean value of the Fermi velocity defined as $v = (2v_\perp + v_3)/3$, cf. Eq. (2). Taking into account Eq. (41) and using the number $\bar{C} = (2C_\perp + C_3)/3$, with $\bar{C} \simeq 0.47$ for TaAs, we obtain another correction to the Fermi velocity which must be added to Eq. (41),

$$
\delta v' = -\frac{g_e^2}{4\pi}\frac{\bar{C} c_{\mathrm{ph}}}{\rho_0 v}\left(\frac{g_{\mathrm{ph}} e_{33}}{c_{\mathrm{ph}}}\right)^2 d\ell. \quad (45)
$$

Since $\bar{C} > 0$, the piezoelectric corrections tend to decrease the Fermi velocities.

5. Piezoelectric vertex correction

One-loop vertex corrections do arise from the piezoelectric coupling, see the diagram in Fig. 5(e). This diagram is studied in detail in Appendix C. We obtain a charge renormalization corresponding to the RG flow of the coupling g_e in Eq. (25). For the $4mm$ crystal class, and using again Eqs. (2) and (16), we obtain

$$
\delta g_e = \frac{C_0}{4\pi\rho_0}\frac{c_{\mathrm{ph}}}{v}\left(\frac{g_e g_{\mathrm{ph}} e_{33}}{c_{\mathrm{ph}}}\right)^2 g_e d\ell, \quad (46)
$$

with $C_0 \simeq 1.40$ for TaAs. Note the factor of $c_{\mathrm{ph}}/v \ll 1$, which is a manifestation of Migdal's theorem for WSMs [72]. The fact that the same coefficient C_0 governs both the vertex correction and the field renormalization, see Eq. (44), is due to a Ward identity for electron-phonon interactions [73]. We also have $\delta g_{\mathrm{ph}} = 0$ because there are no loop corrections in this vertex.

B. RG equations

We now collect the results of Sec. III A. The one-loop RG equations are then given by

$$
\frac{dZ_\psi}{d\ell} = -C_0 \frac{c_{\mathrm{ph}}}{v}\frac{g_e^2}{4\pi v}\frac{g_{\mathrm{ph}}^2 e_{33}^2}{\rho_0 c_{\mathrm{ph}}^2} Z_\psi,
$$
$$
\frac{dZ_\varphi}{d\ell} = -\frac{N g_e^2}{6\pi^2 v} Z_\varphi,
$$
$$
\frac{dv}{d\ell} = \frac{g_e^2}{6\pi^2}\left[1 - \frac{3\pi(C_0 + \bar{C})}{2}\frac{c_{\mathrm{ph}}}{v}\frac{g_{\mathrm{ph}}^2 e_{33}^2}{\rho_0 c_{\mathrm{ph}}^2}\right], \quad (47)
$$
$$
\frac{dg_e}{d\ell} = -\frac{N g_e^3}{12\pi^2 v},
$$
$$
\frac{dg_{\mathrm{ph}}}{d\ell} = -\frac{N g_e^2 g_{\mathrm{ph}}}{12\pi^2 v}.
$$

We note that on effective length scales beyond the mean free path, disorder effects could modify the above RG equations. For $g_{\mathrm{ph}} = 0$, we recover the RG equations in the absence of phonons, in which case the Coulomb vertex g_e is marginally irrelevant and the Fermi velocity increases monotonically as we lower the energy scale. For $g_{\mathrm{ph}} \neq 0$, the vertex correction $\delta g_e/g_e$ due to the piezoelectric interaction gets canceled by the field renormalization $\delta Z_\psi/Z_\psi$ and g_e still decreases with the RG flow. Solving the RG equations numerically with the initial condition set by the parameters for TaAs, we obtain the flow diagram in Fig. 6(a).

However, we find that an instability can arise if the piezoelectric interaction is strong enough to reverse the flow of the Fermi velocity and make it vanish (or become of the order of the phonon velocity) at some finite energy scale. A rough estimate of the condition for this instability is obtained by imposing that $dv/d\ell$ must be negative at the beginning of the RG flow. This requires $\bar{\gamma} > \frac{2w_\gamma}{3\pi(C_0+\bar{C})}\frac{v}{c_{\mathrm{ph}}}$. While C_0, $\bar{C}$, and w_γ are constants of order unity, the factor of velocity ratio $v/c_{\mathrm{ph}} \gg 1$ pushes the critical $\bar{\gamma}$ to a higher value than estimated within the static approximation. Integrating the RG equations numerically, we find that the renormalized velocity does vanish when we enhance the piezoelectric coefficient such that $\bar{\gamma} \simeq 75$, as shown in Fig. 6(b). Therefore, this RG analysis suggests that retardation effects make the WSM phase more stable against a superconducting transition.

IV. PHASE DIAGRAM AND SUPERCONDUCTIVITY

We next perform a self-consistent mean-field analysis to locate superconducting regions in the phase diagram within the static approximation for the total interaction. We develop the mean-field approach in Sec. IV A and study the stability of superconducting phases with singlet or triplet pairing. For small $\bar{\gamma}$, the WSM phase remains stable but will be characterized by a sizable quasiparticle decay rate Γ. We determine the dependence of Γ on temperature and on the energy of the quasiparticle in Sec. V.

A. Mean-field theory

Since pairing involves time-reversed partner states, we consider the effective internode e-e interaction potential
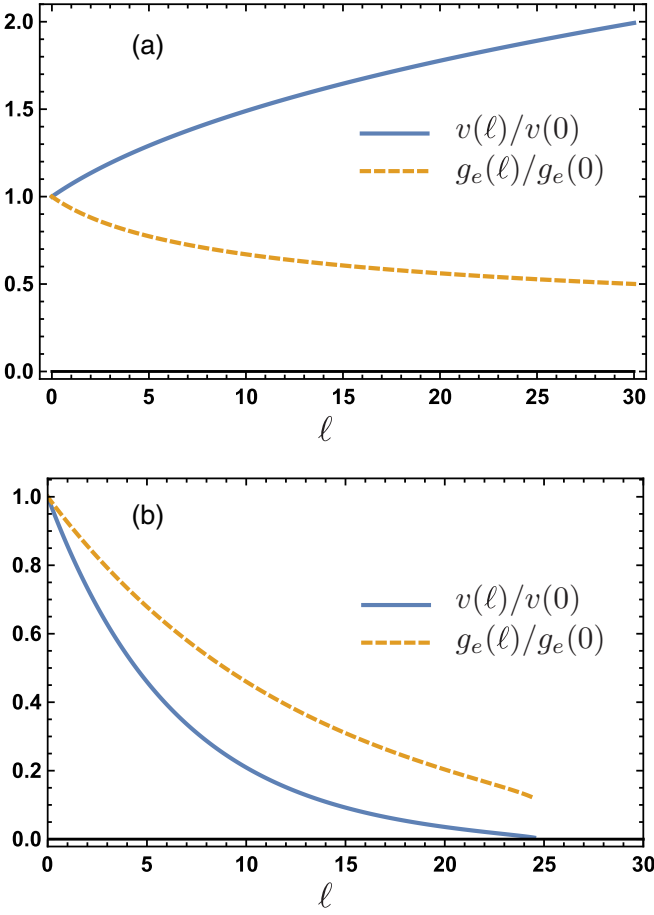
FIG. 6. Renormalized Fermi velocity $v(\ell)$ and Coulomb coupling $g_e(\ell)$ as functions of the RG flow parameter $\ell = \ln(\Lambda_0/\Lambda)$. (a) Flow diagram obtained using the estimated parameters for TaAs, corresponding to $\bar{\gamma} = 0.20$, but considering $2N = 4$ Weyl nodes. (b) Flow diagram obtained by enhancing the piezoelectric coefficient e_{33} to reach $\bar{\gamma} \simeq 75$. Here we stop the RG flow at the scale where the Fermi velocity vanishes, at which point the WSM becomes unstable.

$V_{\text{tot}}(\mathbf{q})$ in Eq. (29) for a pair of nodes ($h = 1, 2$) that are linked by time reversal. The Hamiltonian is then given by

$$H_{\text{eff}} = \sum_{h=1}^{2} \sum_{\mathbf{p}} \psi_h^{\dagger}(\mathbf{p})(v\mathbf{p} \cdot \boldsymbol{\sigma})\psi_h(\mathbf{p})$$
$$+ \frac{1}{V} \sum_{\mathbf{k,p,q}} V_{\text{tot}}(\mathbf{q})\psi_1^{\dagger}(\mathbf{p}+\mathbf{q})\psi_1(\mathbf{p})\psi_2^{\dagger}(\mathbf{k}-\mathbf{q})\psi_2(\mathbf{k}).$$

(48)

We assume the static approximation for the total e-e interaction, as done in the standard BCS theory for the normal-metal-superconductor transition. While phonon-induced retardation effects could be included within Eliashberg theory, we here explore only the static case defined by Eq. (48). We expect to encounter a superconducting phase for $\bar{\gamma} > 1$, see Eq. (34), where the effective interaction V_{tot} will be attractive in all directions and the order parameter should describe s-wave singlet pairing. However, it is worth mentioning that the breaking of spin-rotational invariance by spin-orbit coupling in WSMs blurs the distinction between singlet and triplet

pairing [53]. In fact, a mixing of singlet and triplet components is generic for noncentrosymmetric superconductors [74,75]. With this caveat in mind, we now implement the mean-field approximation for H_{eff} in Eq. (48).

We consider a generic spin-matrix order parameter, $\boldsymbol{\Xi}(\mathbf{k})$, defined by

$$\langle \psi_{1\sigma}(\mathbf{k})\psi_{2\sigma'}(-\mathbf{k}+\mathbf{q})\rangle = \delta_{\mathbf{q},0}\left[\boldsymbol{\Xi}(\mathbf{k})i\sigma_2\right]_{\sigma\sigma'}. \quad (49)$$

The gap function then also corresponds to a complex-valued spin matrix,

$$\boldsymbol{\Delta}(\mathbf{p}) = -\frac{1}{V}\sum_{\mathbf{k}} V_{\text{tot}}(\mathbf{p}-\mathbf{k})\boldsymbol{\Xi}(\mathbf{k}). \quad (50)$$

Using four-component Nambu spinor operators [25],

$$\Psi(\mathbf{p}) = \begin{bmatrix} \psi_1(\mathbf{p}) \\ i\sigma_2\psi_2^{\dagger}(-\mathbf{p}) \end{bmatrix}, \quad \psi_h(\mathbf{p}) = \begin{bmatrix} \psi_{h,\uparrow}(\mathbf{p}) \\ \psi_{h,\downarrow}(\mathbf{p}) \end{bmatrix}, \quad (51)$$

the standard mean-field decoupling scheme yields the Bogoliubov-de-Gennes (BdG) Hamiltonian

$$H_{\text{BdG}} = \sum_{\mathbf{p}}\{\Psi^{\dagger}(\mathbf{p})\mathcal{H}_{\text{BdG}}(\mathbf{p})\Psi(\mathbf{p}) + \text{Tr}[\boldsymbol{\Delta}^{\dagger}(\mathbf{p})\boldsymbol{\Xi}(\mathbf{p})]\},$$

$$\mathcal{H}_{\text{BdG}}(\mathbf{p}) = \begin{bmatrix} v\boldsymbol{\sigma} \cdot \mathbf{p} & \boldsymbol{\Delta}(\mathbf{p}) \\ \boldsymbol{\Delta}^{\dagger}(\mathbf{p}) & -v\boldsymbol{\sigma} \cdot \mathbf{p} \end{bmatrix}. \quad (52)$$

We will now examine the conditions for superconducting phases with singlet vs. triplet pairing.

1. Singlet pairing

For the case of singlet pairing, we write $\boldsymbol{\Delta}(\mathbf{p}) = \Delta_0(\mathbf{p})\sigma_0$ in a gauge where the scalar function $\Delta_0(\mathbf{p})$ is real valued. Diagonalizing $\mathcal{H}_{\text{BdG}}(\mathbf{p})$ in Eq. (52), one finds the eigenvalues $\pm E_s(\mathbf{p})$ with $E_s(\mathbf{p}) = \sqrt{v^2\mathbf{p}^2 + \Delta_0^2(\mathbf{p})}$. The gap equation then follows from Eq. (50) by noting that Eq. (49) is solved by a spin-isotropic matrix, $\boldsymbol{\Xi}(\mathbf{k}) = \frac{\Delta_0(\mathbf{k})}{2E_s(\mathbf{k})}\sigma_0$. Using the averaged interaction potential in Eq. (33) with $\bar{\gamma}$ in Eq. (34), the solution follows by assuming a constant gap function, $\Delta_0(\mathbf{k}) = \Delta_0$, corresponding to s-wave pairing. For $\Delta_0 \neq 0$, with Eq. (36) we arrive at the gap equation

$$1 = -\frac{1-\bar{\gamma}}{4\pi^2}\int_0^b dk\, k^2 \frac{g_e^2}{k^2\sqrt{v^2k^2+\Delta_0^2}}$$
$$= -\frac{\alpha_{\text{eff}}}{\pi}\ln\left(\frac{2vb}{\Delta_0}\right), \quad (53)$$

where the large-momentum cutoff b corresponds to the momentum separation between different Weyl nodes. For $\alpha_{\text{eff}} < 0$, corresponding to $\bar{\gamma} > 1$, we then find the isotropic gap

$$\Delta_0 = 2vb\, e^{-\pi/|\alpha_{\text{eff}}|}. \quad (54)$$

Assuming that Δ_0 has the same sign at both Weyl nodes [6,52], we obtain a topologically trivial gapped superconductor with conventional s-wave singlet pairing. However, it is worth noting again that a finite gap emerges even though v_F vanishes at the Fermi level. Technically, the $1/\mathbf{k}^2$ momentum dependence of the long-range interaction potential compensates the density-of-states factor k^2 in Eq. (53).

2. Nodal-line triplet pairing

We next investigate the possibility of other superconducting phases at $\bar{\gamma} < 1$, where the effective interaction strength is repulsive along certain directions but a significant attractive component exists near the $q_3 = 0$ plane, see Fig. 3(b). A general superconducting order parameter can be written as

$$\boldsymbol{\Delta}(\mathbf{k}) = \Delta_0(\mathbf{k})\sigma_0 + \mathbf{a}(\mathbf{k}) \cdot \boldsymbol{\sigma}, \qquad (55)$$

where $\Delta_0(\mathbf{k})$ is a real scalar function and $\mathbf{a}(\mathbf{k})$ is a complex vector field. For $\mathbf{a} \neq 0$, the superconducting phase has a triplet pairing component [53]. We require that the BdG Hamiltonian (52) preserves time-reversal symmetry, which implies the conditions

$$\Delta_0(-\mathbf{k}) = \Delta_0(\mathbf{k}), \quad \mathbf{a}^*(-\mathbf{k}) = -\mathbf{a}(\mathbf{k}). \qquad (56)$$

We then expand Eq. (55) to first order in $\mathbf{k}$, where time-reversal symmetry and Eq. (56) imply

$$\Delta_0(\mathbf{k}) = \Delta_0, \quad \mathbf{a}(\mathbf{k}) = \boldsymbol{M} \cdot \mathbf{k} + i\mathbf{a}_2. \qquad (57)$$

Here $\boldsymbol{M}$ is a real 3×3 matrix and the vector $\mathbf{a}_2$ also has real entries.

Next, in order to reduce the number of mean-field parameters, we take into account global spin and orbital rotation symmetry around the z axis for tetragonal crystal symmetry. In this argument, we assume that these symmetries are approximately realized even when expanding around the Weyl nodes. This approximation becomes exact if the Weyl points are separated along the z axis in momentum space. Indeed, a state that minimizes the energy should take advantage of the anisotropy in the effective interaction (29). We thus take $\mathbf{a}_2 = a_2\hat{\mathbf{z}}$ and $\boldsymbol{M} = \text{diag}(a_\perp, a_\perp, a_\parallel)$, leaving us with only four mean-field parameters in Eq. (57). For $\Delta_0 = 0$, the eigenvalues of $\mathcal{H}_{\text{BdG}}(\mathbf{k})$ are given by $\pm E_t(\mathbf{k})$ with

$$E_t^2(\mathbf{k}) = v^2\mathbf{k}^2 + a_\perp^2\mathbf{k}_\perp^2 + a_\parallel^2 k_3^2 + a_2^2$$
$$\pm 2|\mathbf{k}_\perp|\sqrt{(v^2 + a_\perp^2)a_2^2 + v^2k_3^2(a_\perp - a_\parallel)^2}. \qquad (58)$$

For $a_2 = 0$, the energy only vanishes at $\mathbf{k} = 0$, and each of the original Weyl nodes splits into two Bogoliubov-Weyl nodes, similar to the result of Ref. [52] for pairing between nodes with opposite chirality. For $a_2 \neq 0$, the spectrum instead exhibits a *nodal ring* in the $k_3 = 0$ plane,

$$|\mathbf{k}_\perp| = \frac{|a_2|}{\sqrt{v^2 + a_\perp^2}}, \quad k_3 = 0. \qquad (59)$$

For a general discussion of noncentrosymmetric nodal superconductors, see Refs. [9,76,77]. Interaction-induced instabilities in nodal-line WSMs have also recently been studied, e.g., in Ref. [78].

The spectrum in Eq. (58) shows that the parameters $a_\parallel$ and $a_\perp$ mainly just renormalize Fermi velocities, without introducing essential new physics. In order to get tractable analytical expressions, we thus consider the case $a_\parallel = a_\perp = 0$ in what follows. In particular, we test whether it is energetically favorable to convert Weyl nodes into the nodal ring in Eq. (59) where the attractive interactions are most pronounced. To that end, self-consistency equations for the order parameters are derived as shown in Appendix D. We arrive at the coupled
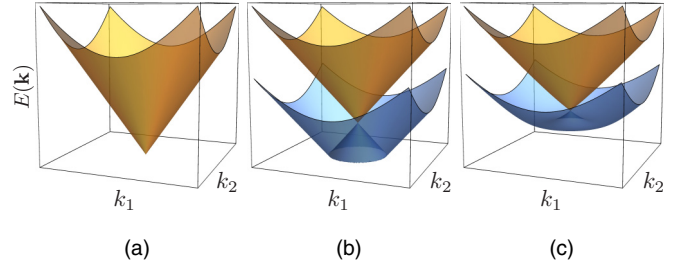

FIG. 7. Schematic representation of the dispersion relations of the two bands for Bogoliubov quasiparticles. Here we set the mean-field parameters $a_\parallel = a_\perp = 0$ and plot the dispersion for $k_3 = 0$. (a) For $a_2 = \Delta_0 = 0$, the Weyl nodes conjugated by time-reversal symmetry are represented as two degenerate Bogoliubov-Weyl nodes. (b) For $\Delta_0 = 0$ but $a_2 \neq 0$, the spectrum is gapless along a nodal line located in the $k_3 = 0$ plane. (c) For $a_2 \neq 0$ and $\Delta_0 \neq 0$, the spectrum is fully gapped.

equations

$$a_2 = \frac{\alpha_{\text{eff}}a_2}{4\pi}\int_0^\pi d\theta \sin\theta[\gamma(\theta) - 1]$$
$$\times (1 + \sin^2\theta)\ln\left(\frac{4v^2b^2}{\Delta_0^2 + a_2^2\cos^2\theta}\right), \qquad (60)$$

and

$$\Delta_0 = \frac{\alpha_{\text{eff}}\Delta_0}{4\pi}\int_0^\pi d\theta \sin\theta[\gamma(\theta) - 1]\ln\left(\frac{4v^2b^2}{\Delta_0^2 + a_2^2\cos^2\theta}\right). \qquad (61)$$

Note that Eq. (60) differs from Eq. (61) by the factor $(1 + \sin^2\theta)$ in the integrand. This factor enhances the contribution from $\theta \approx \pi/2$ where $\gamma(\theta)$ has its maximum. This observation suggests the existence of a parameter window where Eq. (60) has a solution with $a_2 \neq 0$ while $\Delta_0 = 0$ is the only solution to Eq. (61). In Appendix D, we confirm that an intermediate parameter regime exists, $\bar{\gamma}' < \bar{\gamma} < 1$, where such a solution is stable, at least in the absence of disorder. Using TaAs parameters, we find $\bar{\gamma}' \simeq 0.91$. The respective value for the order parameter a_2 is given by Eq. (D8).

Our mean-field approach suggest that superconductivity will be absent for $\bar{\gamma} < \bar{\gamma}'$, where the WSM phase presumably remains stable. We study the quasiparticle lifetime in this regime in Sec. V below. In the intermediate regime $\bar{\gamma}' < \bar{\gamma} < 1$, however, the system becomes a gapless triplet superconductor with internode pairing, where the Weyl nodes split and form a nodal ring located in the $k_3 = 0$ plane. Finally, for $\bar{\gamma} > 1$, the system enters a fully gapped superconducting phase with s-wave singlet pairing, see Sec. IV A 1. The general picture is illustrated in Fig. 7. We emphasize that all these phase transitions can already happen for small absolute values of the fine structure constant $\alpha = g_e^2/(4\pi v)$, within the perturbatively accessible regime.

3. Other competing phases

So far we have discussed superconducting pairing with zero Cooper pair momentum in time-reversal-symmetric WSMs, where a pair of nodes at opposite momenta is conjugated by time reversal. By contrast, in inversion-symmetric

WSMs, the opposite chirality of nodes entails that states with momentum **k** and $-$**k** do not necessarily have opposite spin. In such cases, the type of superconducting order is less clear because pairing between parity-reversed nodes leads to a gapless superconductor [52,53,57]. The authors of Refs. [53,54] have argued that a fully gapped Fulde-Ferrell-Larkin-Ovchinnikov (FFLO) state with intra-node pairing has lower energy than the gapless state. On the other hand, in Ref. [56] an odd-parity BCS state with lower energy than the FFLO state was found. Using our model, pairing between nodes of opposite chirality can also be studied and could allow for a nodal FFLO-type superconducting phase. However, paired states are then not related by any symmetry, and we find it unlikely that a lower energy than for the BCS state in Sec. IV A 1 can be achieved for $\bar{\gamma} > 1$. Moreover, our attractive phonon-mediated interaction favors pairing between time-reversal-conjugated nodes. In Eq. (21), phonons couple to the total electronic density, and projecting H_{pz} onto the Weyl nodes at low energies, we find the same coupling to all nodes. Nonetheless, the process of integrating out high-energy modes could lift this degeneracy, and one pair of Weyl nodes may ultimately have a stronger coupling. The effective e-e interaction used as input in Eq. (48) will then favor a pairing of the time-reversal-conjugated nodes with the strongest coupling, as opposed to some other combination of nodes.

Let us also comment on the possibility of charge density wave (CDW) phases, see Ref. [79]. For the model with short-range attractive interactions in Ref. [79], a CDW instability can only occur at strong coupling. It is straightforward to adapt their calculation to our model with long-range attraction. The mean-field Hamiltonian for the CDW state is essentially as for our singlet pairing state in Sec. IV A 1. The difference is that the four-component spinor is defined as $(\psi_{1\uparrow}, \psi_{1\downarrow}, \psi_{2\uparrow}, \psi_{2\downarrow})^t$, where 1 and 2 now refer to two nodes with opposite chirality and the order parameter is $\langle \psi_1^\dagger(\mathbf{k}) \psi_2(\mathbf{k}) \rangle$. As this CDW order parameter breaks chiral symmetry, it leads to an axion insulator where the axion field is identified with the phase of the charge density wave. However, in our setting, this type of order depends on the interaction between nodes which are not related by any symmetry. By the above argument, this state should have higher energy than the BCS state.

In addition, there may be other phases at intermediate coupling, $\bar{\gamma} \lesssim 1$. One particularly intriguing possibility concerns phases that break time-reversal symmetry spontaneously, e.g., a $p + ip$ superconductor. We leave the exploration of such phases to future work.

V. QUASIPARTICLE LIFETIME

We next address the temperature and momentum dependence of the on-shell quasiparticle decay rate, $\Gamma(\mathbf{p}, T)$, caused by the piezoelectric e-ph coupling. We assume that $\bar{\gamma}$ is so small that interaction-induced instabilities are absent. We show below that in this WSM phase, the e-ph interaction is responsible for a rather large quasiparticle decay rate, scaling as $\Gamma \sim T/\ln(b/|\mathbf{p}|)$ at low-to-intermediate temperatures with $T \gg c_{ph}|\mathbf{p}|$. To ease notation, we again employ Eqs. (2) and (16).

A. General expression for the decay rate

Diagrammatically, the lowest-order electronic self-energy is represented by Figs. 5(a) and 5(d). Since the rainbow diagram in Fig. 5(a) is a real-valued Hartree-Fock diagram, it does not contribute to the decay rate. The e-e interaction only produces a finite decay rate at higher orders and beyond the Hartree-Fock approximation. In order to compute Γ, we therefore study the self-energy due to e-ph interactions, Σ_{ep}, see Fig. 5(d). The rate follows from the imaginary part of $\Sigma_{ep}(E, \mathbf{p})$, which in turn is obtained by analytic continuation $i\omega \to E + i0^+$, see, e.g., Ref. [80].

To be specific, we study the lifetime of a Weyl quasiparticle in the state $|\mathbf{p}, \mu = +\rangle$ with momentum $\mathbf{p}$, taken from the positive-energy ($\mu = +$) band. We consider the on-shell case, $E = v|\mathbf{p}|$. The quasiparticle decay rate is then given by

$$\Gamma(\mathbf{p}, T) = -2 \, \mathrm{Im} \, \langle \mathbf{p}, +|\Sigma_{ep}(\mathbf{p})|\mathbf{p}, +\rangle. \tag{62}$$

Let us now make use of the results of Sec. III A 4 and Appendix B. We first observe that the decay rate must vanish right at the Weyl point, $\Gamma(\mathbf{p} = 0, T) = 0$, since then momentum and energy conservation cannot be satisfied for any phonon momentum $\mathbf{q} \neq 0$. For $|\mathbf{p}| \neq 0$, it is convenient to rescale $\mathbf{q} = \xi|\mathbf{p}|\hat{\mathbf{q}}$ with the dimensionless parameter ξ. Denoting the integration angles by $\theta_\mathbf{q}$ and $\phi_\mathbf{q}$, and using $\langle \mathbf{p}, +|\boldsymbol{\sigma} \cdot \mathbf{q}|\mathbf{p}, +\rangle = |\mathbf{q}|\hat{\mathbf{q}} \cdot \hat{\mathbf{p}}$, we find

$$\Gamma(\mathbf{p}, T) = \frac{g_e^2 g_{ph}^2 c_{ph}^2 |\mathbf{p}|}{8\pi^2 \rho_0} \int_0^\infty d\xi\, \xi^2 \int_0^\pi d\theta_\mathbf{q} \sin\theta_\mathbf{q} \int_{-\pi}^\pi d\phi_\mathbf{q}\, \gamma(\hat{\mathbf{q}}) \sum_{s=\pm} \left\{ F_1^{(s)}(|\mathbf{p}|, \xi, \hat{\mathbf{q}} \cdot \hat{\mathbf{p}}) \delta[(v + s c_{ph}\xi)^2 - v^2(1 + \xi^2 + 2\xi\hat{\mathbf{q}} \cdot \hat{\mathbf{p}})] \right.$$

$$\left. + F_2^{(s)}(|\mathbf{p}|, \xi, \hat{\mathbf{q}} \cdot \hat{\mathbf{p}})\, \delta\big[v^2(1 - s\sqrt{1 + \xi^2 + 2\xi\hat{\mathbf{q}} \cdot \hat{\mathbf{p}}})^2 - c_{ph}^2 \xi^2\big] \right\}, \tag{63}$$

$$F_1^{(s=\pm)} = g_1^{(s)}(\xi) \frac{n_B(s c_{ph}|\mathbf{p}|\xi)}{s c_{ph}\xi}[2v + s c_{ph}\xi + v\xi\hat{\mathbf{q}} \cdot \hat{\mathbf{p}}],$$

$$F_2^{(s=\pm)} = -g_2^{(s)}(\xi, \hat{\mathbf{q}} \cdot \hat{\mathbf{p}}) \frac{n_F(sv|\mathbf{p}|\sqrt{1 + \xi^2 + 2\xi\hat{\mathbf{q}} \cdot \hat{\mathbf{p}}})}{sv\sqrt{1 + \xi^2 + 2\xi\hat{\mathbf{q}} \cdot \hat{\mathbf{p}}}}[v\sqrt{1 + \xi^2 + 2\xi\hat{\mathbf{q}} \cdot \hat{\mathbf{p}}} + sv(1 + \xi\hat{\mathbf{q}} \cdot \hat{\mathbf{p}})], \tag{64}$$

with $\gamma(\hat{\mathbf{q}})$ in Eq. (27), $n_F(\omega) = 1/(e^{\beta\omega} + 1)$, $n_B(\omega) = 1/(e^{\beta\omega} - 1)$, and

$$g_1^{(-)} = \operatorname{sgn}\left(1 - \frac{c_{\text{ph}}\xi}{v}\right), \quad g_1^{(+)} = g_2^{(-)} = 1,$$

$$g_2^{(+)} = \operatorname{sgn}(1 - \sqrt{1 + \xi^2 + 2\xi\hat{\mathbf{q}} \cdot \hat{\mathbf{p}}}). \quad (65)$$

B. Zero-temperature limit

Let us first address the $T = 0$ case, where only $F_1^{(-)}$ in Eq. (64) yields a finite contribution to the decay rate,

$$\Gamma(\mathbf{p}, T = 0) = \frac{g_e^2 g_{\text{ph}}^2 c_{\text{ph}} |\mathbf{p}|}{4\pi^2 \rho_0 v} \int_0^\pi d\theta_{\mathbf{q}} \sin\theta_{\mathbf{q}} \int_{-\pi}^\pi d\phi_{\mathbf{q}}$$

$$\times \gamma(\hat{\mathbf{q}})[1 - (\hat{\mathbf{q}} \cdot \hat{\mathbf{p}})^2]\Theta(-\hat{\mathbf{q}} \cdot \hat{\mathbf{p}}), \quad (66)$$

where $\Theta(x)$ is the Heaviside step function. Since the integral in Eq. (66) is finite, we conclude that the $T = 0$ rate scales as $\Gamma \sim |\mathbf{p}|$ when approaching the Weyl point.

C. Finite temperatures

Next we consider low but finite temperatures in the regime

$$c_{\text{ph}}|\mathbf{p}| \ll T \ll \min(v|\mathbf{p}|, c_{\text{ph}}b). \quad (67)$$

The dominant contributions to the decay rate (63) then stem from the $F_1^{(\pm)}$ terms in Eq. (63), where the Bose factors can be approximated by $n_B \simeq \pm T/(c_{\text{ph}}|\mathbf{p}|\xi)$, respectively. We then obtain

$$\Gamma(\mathbf{p}, T) = \frac{g_e^2 g_{\text{ph}}^2 T}{4\pi^2 \rho_0 v} \int_0^\pi d\theta_{\mathbf{q}} \sin\theta_{\mathbf{q}} \int_{-\pi}^\pi d\phi_{\mathbf{q}}$$

$$\times \frac{\gamma(\hat{\mathbf{q}})}{|\hat{\mathbf{q}} \cdot \hat{\mathbf{p}}|}[1 - (\hat{\mathbf{q}} \cdot \hat{\mathbf{p}})^2]\Theta(-\hat{\mathbf{q}} \cdot \hat{\mathbf{p}}). \quad (68)$$

However, the integral (68) diverges logarithmically at the boundary of the hemisphere $\hat{\mathbf{q}} \cdot \hat{\mathbf{p}} < 0$, corresponding to small-angle scattering processes with $\xi \to 0$. This infrared divergence is related to the long-range character of the piezoelectric interaction. Note that so far we have always assumed $T = 0$, with the Fermi energy located right at the Weyl point. In that case, the unscreened Coulomb potential can be used. For the finite-temperature quasiparticle decay rate, we need to be more careful since also finite-energy states within an energy window of width $\approx T$ around the Weyl point are involved. For such states, the long-range Coulomb interaction is modified by dynamic screening [38,81]. By taking into account screening, we now show that the above divergence is indeed removed.

Dynamic screening of the Coulomb interaction can be included by replacing the permittivity according to [25]

$$\varepsilon \mapsto \varepsilon(q) = \left[1 - \frac{g_e^2}{\mathbf{q}^2}\Pi(q)\right]\varepsilon, \quad (69)$$

where $\Pi(q)$ is the polarization function. Within the standard random-phase approximation, we take $\Pi(q)$ to be the noninteracting polarization bubble, cf. Fig. 5(c), where the $T = 0$ limit of the polarization function yields a good description for the temperature regime (67). A temperature dependence of the decay rate is then generated only by e-ph interactions.

(We note that disorder effects could modify our expressions.) To obtain the dominant terms contributing to $\Gamma(\mathbf{p}, T)$ in this regime, the logarithmic on-shell term calculated in Refs. [38,82] suffices,

$$\Pi(q) \simeq -\frac{N|\mathbf{q}|^2}{6\pi^2 v} \ln(2b/|\mathbf{q}|), \quad (70)$$

where b serves as large-momentum cutoff again. Note that two factors of ε^{-1} appear in Eq. (68), associated with either g_e^2 or g_{ph}^2. One can identify these two factors with the two wiggly lines in the self-energy diagram in Fig. 5(d). Dressing both lines with the polarization bubble, we arrive at a modified version of Eq. (68) which takes into account screening,

$$\Gamma(\mathbf{p}, T) = \frac{g_e^2 g_{\text{ph}}^2 T}{4\pi^2 \rho_0 v} \int_0^\pi d\theta_{\mathbf{q}} \sin\theta_{\mathbf{q}} \int_{-\pi}^\pi d\phi_{\mathbf{q}}$$

$$\times \frac{\gamma(\hat{\mathbf{q}})}{|\hat{\mathbf{q}} \cdot \hat{\mathbf{p}}|} \frac{1 - (\hat{\mathbf{q}} \cdot \hat{\mathbf{p}})^2}{\left[1 + \frac{Ng_e^2}{6\pi^2 v} \ln\left(\frac{1}{|\hat{\mathbf{q}} \cdot \hat{\mathbf{p}}|} \frac{b}{|\mathbf{p}|}\right)\right]^2}\Theta(-\hat{\mathbf{q}} \cdot \hat{\mathbf{p}}). \quad (71)$$

Using $|\mathbf{p}| \ll b$, the regime (67) is therefore characterized by a quasiparticle decay rate which scales as

$$\Gamma(\mathbf{p}, T) \sim \frac{T}{\ln(b/|\mathbf{p}|)}. \quad (72)$$

We observe that $\Gamma(\mathbf{p}, T)$ vanishes for $|\mathbf{p}| \to 0$, as expected from kinematic constraints. However, the slow logarithmic scaling with $|\mathbf{p}|$, together with the linear-T dependence, suggests that the quasiparticle lifetime of Weyl fermions is significantly reduced by the piezoelectric e-ph interaction, even when one stays in the very close vicinity of a Weyl point.

VI. CONCLUDING REMARKS

In this work we have studied the long-range attractive interactions mediated by the piezoelectric electron-phonon coupling in undoped noncentrosymmetric Weyl semimetals. These interactions exhibit a significant angular dependence and compete with the repulsive Coulomb interactions. This competition is mainly governed by the dimensionless piezoelectric coupling strength $\bar{\gamma}$ in Eq. (34). Within a static approximation for the effective e-e interaction, we find that for $\bar{\gamma} > 1$ the attractive interactions outweigh the repulsive Coulomb part. We then predict a conventional BCS superconductor phase with spin-singlet s-wave pairing, even though the normal density of states vanishes at the Fermi level. We have performed a mean-field analysis to study this state in some detail.

According to our rough estimate $\bar{\gamma} \approx 0.20$ for TaAs, see Sec. II E, the above BCS scenario is probably hard to encounter in TaAs. However, for $\bar{\gamma} < 1$, other, and even more interesting, interacting phases may be stabilized. For example, our analysis in Sec. IV A suggests that a nodal-ring gapless spin-triplet superconductor will be realized for intermediate values of $\bar{\gamma}$. Our RG analysis also shows that the critical values for $\bar{\gamma}$ where superconducting instabilities are found can be pushed upwards by retardation effects.

For small $\bar{\gamma}$, we expect that the Weyl semimetal phase remains stable. Nonetheless, the piezoelectric coupling should leave a clear experimental trace in the quasiparticle decay rate at finite temperature. In particular, we find that this rate scales

as $\Gamma \sim T/\ln(b/|\mathbf{p}|)$ at low-to-intermediate T. Albeit $\Gamma = 0$ right at a Weyl point ($\mathbf{p} = 0$), the weak logarithmic scaling with $|\mathbf{p}|$ suggests that the quasiparticle lifetime will be rather short even for very small (but finite) $|\mathbf{p}|$. In any case, we hope that future theoretical and experimental research will continue to study the interesting consequences of piezoelectric couplings in Weyl semimetals.

APPENDIX A: ELECTRONIC SELF-ENERGY FROM COULOMB INTERACTIONS

Here we provide details concerning the electronic self-energy correction from Coulomb interactions, see Sec. III A 1. Using Eq. (5) and performing the internal frequency integration in Eq. (39), we obtain

$$\Sigma_{ee}(i\omega, \mathbf{p}) = \frac{g_e^2}{2} \int \frac{d^3\mathbf{q}}{(2\pi)^3} \frac{1}{\mathbf{q}^2}$$
$$\times \left[-\sigma_0 + \frac{v_\perp(\mathbf{p}_\perp + \mathbf{q}_\perp) \cdot \boldsymbol{\sigma}_\perp + v_3(p_3 + q_3)\sigma_3}{E(\mathbf{p} + \mathbf{q})} \right], \tag{A1}$$

which is independent of the frequency ω. We now expand Eq. (A1) for $|\mathbf{p}| \ll |\mathbf{q}|$. For $\mathbf{p} = 0$, one finds a nonuniversal constant that can be absorbed by renormalization of the chemical potential. The renormalized value of the chemical potential is then assumed to be aligned with the Weyl node. Universal RG contributions appear at the first order in $\mathbf{p}$. For

instance, from terms linear in p_3, we get a contribution of the form

$$\Sigma_{ee}(p_3) = \frac{g_e^2}{2} v_3 p_3 \sigma_3 \int \frac{d^3\mathbf{q}}{(2\pi)^3} \frac{v_\perp^2 \mathbf{q}_\perp^2}{\mathbf{q}^2 E^3(\mathbf{q})}, \tag{A2}$$

where momentum-shell integration yields the self-energy correction

$$\delta\Sigma_{ee}(p_3) = \frac{g_e^2}{8\pi^2} \eta_3 p_3 \sigma_3 d\ell,$$
$$\eta_3 = \frac{v_3}{v_\perp} \int_0^\pi d\theta \frac{\sin^3\theta}{[\sin^2\theta + (v_3/v_\perp)^2 \cos^2\theta]^{3/2}}. \tag{A3}$$

Self-energy terms $\sim \mathbf{p}_\perp$ follow in a similar manner with η_3 replaced by $\eta_\perp = 4v_\perp/(3v_3)$. For the isotropic case (2), we then find $\eta_\perp = \eta_3 = 4/3$. The complete linear-in-$\mathbf{p}$ self-energy correction after momentum-shell integration is given by Eq. (40).

APPENDIX B: ELECTRON SELF-ENERGY FROM E-PH INTERACTIONS

Next we turn to the self-energy $\Sigma_{ep}(p)$ due to piezoelectric interactions, see Sec. III A 4. The leading term arises from the diagram in Fig. 5(d),

$$\Sigma_{ep}(p) = -g_e^2 g_{ph}^2 \sum_{ijk} \sum_{lmn} e_{ijk} e_{lmn}$$
$$\times \int \frac{d^4q}{(2\pi)^4} \frac{q_i q_j q_l q_m}{|\mathbf{q}|^4} D_{kn}(q) \mathbb{G}(p + q), \tag{B1}$$

with the phonon propagator in Eq. (14) and the electronic GF in Eq. (5). Performing the internal frequency integration, we obtain

$$\Sigma_{ep}(i\omega, \mathbf{p}) = -\frac{g_e^2 g_{ph}^2}{4\rho_0} \sum_J \sum_{ijk} \sum_{lmn} e_{ijk} e_{lmn} \int \frac{d^3\mathbf{q}}{(2\pi)^3} \frac{q_i q_j q_l q_m \epsilon_k^J(\mathbf{q}) \epsilon_n^J(-\mathbf{q})}{|\mathbf{q}|^4 \Omega_J(\mathbf{q}) E(\mathbf{p} + \mathbf{q})}$$
$$\times \sum_\pm \frac{[i\omega \pm \Omega_J(\mathbf{q})]\sigma_0 + v_\perp(\mathbf{p}_\perp + \mathbf{q}_\perp) \cdot \boldsymbol{\sigma}_\perp + v_3(p_3 + q_3)\sigma_3}{\pm i\omega + \Omega_J(\mathbf{q}) + E(\mathbf{p} + \mathbf{q})}. \tag{B2}$$

We now integrate out all phonon modes within the high-energy shell. For $4mm$ crystal symmetry and using Eqs. (2) and (16), to linear order in p, we find the correction

$$\delta\Sigma_{ep}(p) = -g_e^2 \left(\frac{i\zeta_0 \omega}{v} \sigma_0 + \zeta_\perp \mathbf{p}_\perp \cdot \boldsymbol{\sigma}_\perp + \zeta_3 p_3 \sigma_3 \right) d\ell, \tag{B3}$$

with, cf. Eq. (30),

$$\zeta_0 = \frac{C_0}{\rho_0} \left(\frac{g_{ph} e_{33}}{c_{ph}} \right)^2 \frac{c_{ph}}{v},$$
$$C_0 = \frac{1}{15\pi} \left(10A^2 + 4AB + 4A + 2B^2 + 3 \right) \simeq 1.40. \tag{B4}$$

The terms $\sim \mathbf{p}$ in Eq. (B3) involve dimensionless numbers $\zeta_\perp$ and ζ_3 defined as in Eq. (B4) but with $C_0 \to C_{\perp,3}$, where

$$C_\perp = \frac{1}{105\pi} (14A^2 + 12AB + 12A + 6B^2 + 15),$$
$$C_3 = \frac{1}{105\pi} (42A^2 + 4AB + 4A + 2B^2 - 9). \tag{B5}$$

Using Eq. (30) with the parameters quoted in Sec. II E, we find $C_\perp \simeq 0.29$ and $C_3 \simeq 0.83$. The self-energy corrections are summarized in Eq. (43).

APPENDIX C: VERTEX CORRECTIONS

Here we provide details about the vertex correction due to the diagram in Fig. 5(e), see Sec. III A 5. We define the

three-point function with fermions in the band basis

$$\Lambda_{\mu\mu'}(x, x', x'') = \langle T\psi_\mu(x)\psi_{\mu'}^\dagger(x')\varphi(x'')\rangle. \tag{C1}$$

The free boson propagator is $D_\varphi(x) = \langle\varphi(x)\varphi(0)\rangle$. In momentum space, $D_\varphi(q) = -|\mathbf{q}|^{-2}$.

The three-point function at tree level is obtained by perturbation theory to first order in g_e. Taking the Fourier transform $\Lambda_{\sigma\sigma'l}(p, p', q) = \int d^4x d^4x' d^4x'' e^{-ipx-ip'x'-iqx''} \Lambda_{\sigma\sigma'l}(x, x', x'')$, we find

$$\Lambda_{\mu\mu'}^{(1)}(p, p', q) = ig_e[\mathcal{U}^\dagger(\mathbf{p})\mathcal{U}(\mathbf{p}+\mathbf{q})]_{\mu\mu'}G_\mu(p)G_{\mu'}(p+q)D_\varphi(q)(2\pi)^4\delta(p'+p+q). \tag{C2}$$

The vertex correction at the one-loop level appears at order $g_e^3 g_{\rm ph}^2$:

$$\Lambda_{\mu\mu'}^{(3,2)}(p, p', q) = -ig_e^3 g_{\rm ph}^2 D_\varphi(q)(2\pi)^4\delta(p'+p+q)\sum_{amb}\sum_{rns}e_{amb}e_{rns}$$

$$\times \sum_{\mu''\mu'''}\int\frac{d^4q'}{(2\pi)^4}\frac{q'_a q'_b q'_r q'_s}{|\mathbf{q'}|^4}D_{mn}(q')G_\mu(p)G_{\mu''}(p-q')G_{\mu'''}(p+q-q')G_{\mu'}(p+q)$$

$$\times [\mathcal{U}^\dagger(\mathbf{p})\mathcal{U}(\mathbf{p}-\mathbf{q'})]_{\mu\mu''}[\mathcal{U}^\dagger(\mathbf{p}-\mathbf{q'})\mathcal{U}(\mathbf{p}+\mathbf{q}-\mathbf{q'})]_{\mu''\mu'''}[\mathcal{U}^\dagger(\mathbf{p}+\mathbf{q}-\mathbf{q'})\mathcal{U}(\mathbf{p}+\mathbf{q})]_{\mu'''\mu'}, \tag{C3}$$

with the phonon propagator in Eq. (15) with $q' = (i\nu', \mathbf{q'})$.

At low energies, all external four-momenta can be assumed small against q'. The integral over the internal frequency ν' then defines the quantities

$$I_{\mu''} = \int_{-\infty}^{+\infty}\frac{d\nu'}{2\pi}\left[\frac{1}{i\nu'-\Omega_J(\mathbf{q'})}-\frac{1}{i\nu'+\Omega_J(\mathbf{q'})}\right]\frac{1}{i\nu-i\nu'-\mu''E(\mathbf{p}-\mathbf{q'})}\frac{1}{i\nu+i\omega-i\nu'-\mu''E(\mathbf{p}+\mathbf{q}-\mathbf{q'})}. \tag{C4}$$

Performing the frequency integral, we obtain

$$I_\pm = -\frac{1}{[i\nu\mp\Omega_J(\mathbf{q'})\mp E(\mathbf{p}-\mathbf{q'})][i\nu+i\omega\mp\Omega_J(\mathbf{q'})\mp E(\mathbf{p}+\mathbf{q}-\mathbf{q'})]}. \tag{C5}$$

We now effectively set the external four-momenta to zero, $p, q \to 0$, which results in $I_\pm = -1/[\Omega_J(\mathbf{q'}) + E(\mathbf{q'})]^2$. In this limit, $\mathcal{U}(\mathbf{p}-\mathbf{q'})\mathcal{U}^\dagger(\mathbf{p}+\mathbf{q}-\mathbf{q'}) \to \sigma_0$, and we arrive at

$$\Lambda_{\mu\mu'l}^{(3)}(p, p', q) = \frac{ig_e^3 g_{\rm ph}^2}{2\rho_0}[\mathcal{U}^\dagger(\mathbf{p})\mathcal{U}(\mathbf{p}+\mathbf{q})]_{\mu\mu'}G_\mu(p)G_{\mu'}(p+q)D_\varphi(q)(2\pi)^4\delta(p'+p+q)$$

$$\times \sum_J\sum_{amb}\sum_{rns}e_{amb}e_{rns}\int\frac{d^3\mathbf{q'}}{(2\pi)^3}\frac{q'_a q'_b q'_r q'_s}{|\mathbf{q'}|^4}\frac{\epsilon_m^J(\mathbf{q'})\epsilon_n^J(-\mathbf{q'})}{\Omega_J(\mathbf{q'})[\Omega_J(\mathbf{q'})+E(\mathbf{q'})]^2}. \tag{C6}$$

At this point, we compute the one-loop contribution to the RG equations by integrating over phonon modes with momenta within the high-energy momentum shell. The correction corresponds to a charge renormalization and hence to a renormalization of the coupling g_e in Eq. (25). We find

$$\delta g_e = \frac{g_e^3 g_{\rm ph}^2}{2\rho_0}\sum_J\int\frac{d^3\mathbf{q}}{(2\pi)^3}\left|\sum_{jkl}e_{jkl}\frac{q_j q_k}{|\mathbf{q}|^2}\epsilon_l^J(\mathbf{q})\right|^2\frac{1}{\Omega_J(\mathbf{q})[\Omega_J(\mathbf{q})+E(\mathbf{q})]^2}. \tag{C7}$$

For the case of TaAs, with the simplifications in Eqs. (2) and (16), one can then employ similar steps as in Appendices A and B. We thereby arrive at Eq. (46).

APPENDIX D: ON TRIPLET PAIRING

In this Appendix, we provide details concerning the solution of the self-consistency equations in Sec. IV A 2 for the triplet pairing case, keeping only Δ_0 and a_2 as free parameters. The self-consistency equations are given by

$$\Delta_0 = -\frac{1}{2V}\sum_{\mathbf{k}}V_{\rm tot}(\mathbf{k}){\rm Tr}[\mathbf{\Xi}(\mathbf{k})],$$

$$a_2 = -\frac{1}{2V}\sum_{\mathbf{k}}V_{\rm tot}(\mathbf{k}){\rm ImTr}[\mathbf{\Xi}(\mathbf{k})\sigma_3]. \tag{D1}$$

Now suppose that $\mathcal{H}_{\rm BdG}(\mathbf{k})$ is diagonalized by the unitary transformation $\Psi(\mathbf{k}) = U(\mathbf{k})\tilde{\Psi}(\mathbf{k})$, with eigenvalues ordered as $[E_1(\mathbf{k}), -E_1(\mathbf{k}), -E_2(\mathbf{k}), E_2(\mathbf{k})]$. For an arbitrary 2×2 matrix W, we can use the auxiliary relation

$${\rm Tr}[\mathbf{\Xi}(\mathbf{k})W] = -\sum_{\lambda=2,3}[U^\dagger(\mathbf{k})\tau^- W U(\mathbf{k})]_{\lambda\lambda}, \tag{D2}$$

where $\tau^\pm = \tau_x \pm i\tau_y$ and Pauli matrices $\tau_{x,y,z}$ act in Nambu space. The self-consistency equations (D1) then reduce to

$$\Delta_0 = \frac{1}{2}\sum_{\lambda=2,3}\int\frac{d^3\mathbf{k}}{(2\pi)^2}V_{\rm tot}(\mathbf{k})[U^\dagger(\mathbf{k})\tau^-\sigma_0 U(\mathbf{k})]_{\lambda\lambda},$$

$$a_2 = \frac{1}{2}\sum_{\lambda=2,3}\int\frac{d^3\mathbf{k}}{(2\pi)^2}V_{\rm tot}(\mathbf{k}){\rm Im}[U^\dagger(\mathbf{k})\tau^-\sigma_3 U(\mathbf{k})]_{\lambda\lambda}, \tag{D3}$$

where the integration domain is the ball $0 < |\mathbf{k}| < b$. Defining the function

$$R(x, \theta) = \sum_{\pm} \frac{a_2 \pm x \sin \theta}{\sqrt{a_2^2 \mp 2a_2 x \sin \theta + \Delta_0^2 + x^2}}, \quad \text{(D4)}$$

the above equation for a_2 takes the form

$$a_2 = \frac{\alpha}{4\pi} \int_0^{vb} dx \int_0^{\pi} d\theta \sin \theta \, R(x, \theta) [\gamma(\theta) - 1], \quad \text{(D5)}$$

where $\alpha = g_e^2 / (4\pi v)$. Performing the integral over x and assuming a_2, $\Delta_0 \ll vb$, we obtain Eq. (60). In a similar fashion, we obtain the equation for Δ_0 in Eq. (61).

Setting $\Delta_0 = 0$ and substituting the form of $\gamma(\theta)$ in Eq. (32), we get from Eq. (60)

$$1 = \frac{\alpha}{2\pi} \int_0^{\pi} d\theta \sin \theta [\gamma(\theta) - 1](1 + \sin^2 \theta) \ln \left| \frac{2vb}{a_2 \cos \theta} \right|$$

$$= -\frac{\alpha}{2\pi} \left[L_1(\bar{\gamma}) + L_2(\bar{\gamma}) \ln \left(\frac{a_2}{2vb} \right) \right]. \quad \text{(D6)}$$

We here define the linear functions $L_{1,2}(\bar{\gamma})$ as

$$L_1(\bar{\gamma}) = \frac{34}{9} - \frac{\bar{\gamma}}{w_\gamma} \left(\frac{256A^2}{75} + \frac{5408AB}{11025} + \frac{5408A}{11025} \right.$$

$$\left. + \frac{2704B^2}{11025} + \frac{146}{1225} \right),$$

$$L_2(\bar{\gamma}) = -\frac{10}{3} + \frac{\bar{\gamma}}{w_\gamma} \left(\frac{18}{35} + \frac{1}{5} 12A^2 - \frac{88AB}{105} - \frac{88A}{105} - \frac{44B^2}{105} \right), \quad \text{(D7)}$$

with $w_\gamma \simeq 4.40$ in Eq. (35). Solving for a_2, we obtain

$$a_2 = 2vb \exp \left(-\frac{2\pi + \alpha L_1}{\alpha L_2} \right). \quad \text{(D8)}$$

For $\alpha \lesssim 1$ and $\bar{\gamma} \lesssim 1$, the constraint $a_2 < 2vb$ simplifies to $L_2(\bar{\gamma}) > 0$. In order to obtain a nontrivial solution for a_2, this in turn requires that

$$\bar{\gamma} > \bar{\gamma}' = \frac{175 w_\gamma}{126A^2 + 44AB + 44A + 22B^2 + 27}. \quad \text{(D9)}$$

For TaAs parameters, Eq. (D9) yields $\bar{\gamma}' \simeq 0.91$.

[1] S. Jia, S. Y. Xu, and M. Z. Hasan, Nat. Mater. **15**, 1140 (2016).

[2] B. Yan and C. Felser, Annu. Rev. Condens. Matter Phys. **8**, 337 (2017).

[3] M. Z. Hasan, S. Y. Xu, I. Belopolski, and S. M. Huang, Annu. Rev. Condens. Matter Phys. **8**, 289 (2017).

[4] G. Volovik, *The Universe in a Helium Droplet* (Clarendon, London, 2003).

[5] A. A. Burkov, Nat. Mater. **15**, 1145 (2016).

[6] P. Hosur and X. Qi, C. R. Phys. **14**, 857 (2013).

[7] A. A. Burkov, J. Phys.: Condens. Matter **27**, 113201 (2015).

[8] A. A. Burkov, Annu. Rev. Condens. Matter Phys. **9**, 359 (2018).

[9] N. P. Armitage, E. J. Mele, and A. Vishwanath, Rev. Mod. Phys. **90**, 015001 (2018).

[10] M. N. Ali, J. Xiong, S. Flynn, J. Tao, Q. D. Gibson, L. M. Schoop, T. Liang, N. Haldolaarachchige, M. Hirschberger, N. Ong *et al.*, Nature **514**, 205 (2014).

[11] S. A. Parameswaran, T. Grover, D. A. Abanin, D. A. Pesin, and A. Vishwanath, Phys. Rev. X **4**, 031035 (2014).

[12] Z. Song, J. Zhao, Z. Fang, and X. Dai, Phys. Rev. B **94**, 214306 (2016).

[13] P. Rinkel, P. L. S. Lopes, and I. Garate, Phys. Rev. Lett. **119**, 107401 (2017).

[14] D. Liu and J. Shi, Phys. Rev. Lett. **119**, 075301 (2017).

[15] J. S. Gordon and H. Y. Kee, Phys. Rev. B **97**, 195106 (2018).

[16] P. Rinkel, P. L. S. Lopes, and I. Garate, Phys. Rev. B **99**, 144301 (2019).

[17] J. Coulter, G. B. Osterhoudt, C. A. C. Garcia, Y. Wang, V. Plisson, B. Shen, N. Ni, K. S. Burch, and P. Narang, arXiv:1903.07550.

[18] C. X. Liu, P. Ye, and X.-L. Qi, Phys. Rev. B **87**, 235306 (2013).

[19] A. Cortijo, Y. Ferreiros, K. Landsteiner, and M. A. H. Vozmediano, Phys. Rev. Lett. **115**, 177202 (2015).

[20] H. Shapourian, T. L. Hughes, and S. Ryu, Phys. Rev. B **92**, 165131 (2015).

[21] D. I. Pikulin, A. Chen, and M. Franz, Phys. Rev. X **6**, 041021 (2016).

[22] A. G. Grushin, J. W. F. Venderbos, A. Vishwanath, and R. Ilan, Phys. Rev. X **6**, 041046 (2016).

[23] M. M. Möller, G. A. Sawatzky, M. Franz, and M. Berciu, Nat. Commun. **8**, 2267 (2017).

[24] Y. Ferreiros, Y. Kedem, E. J. Bergholtz, and J. H. Bardarson, Phys. Rev. Lett. **122**, 056601 (2019).

[25] G. D. Mahan, *Many Particle Physics* (Kluwer, Amsterdam 2000).

[26] P. Y. Yu and M. Cardona, *Fundamentals of Semiconductors: Physics and Materials Properties*, 4th edition (Springer, Berlin, 2010).

[27] F. Giustino, Rev. Mod. Phys. **89**, 015003 (2017).

[28] D. Varjas, A. G. Grushin, R. Ilan, and J. E. Moore, Phys. Rev. Lett. **117**, 257601 (2016).

[29] D. Vanderbilt, J. Phys. Chem. Solids **61**, 147 (2000).

[30] A. Cortijo, D. Kharzeev, K. Landsteiner, and M. A. H. Vozmediano, Phys. Rev. B **94**, 241405(R) (2016).

[31] G. D. Mahan, in *Polarons in Ionic Crystals and Polar Semiconductors*, edited by J. T. Devreese (North-Holland, Amsterdam, 1972), p. 553.

[32] P. Vogl, Phys. Rev. B **13**, 694 (1976).

[33] M. Buchhold, S. Diehl, and A. Altland, Phys. Rev. Lett. **121**, 215301 (2018).

[34] A. A. Abrikosov, J. Low. Temp. Phys. **8**, 315 (1972).

[35] H. Isobe and N. Nagaosa, Phys. Rev. B **86**, 165127 (2012).

[36] H. Isobe and N. Nagaosa, Phys. Rev. B **87**, 205138 (2013).

[37] B.-J. Yang, E.-G. Moon, H. Isobe, and N. Nagaosa, Nat. Phys. **10**, 774 (2014).

[38] R. E. Throckmorton, J. Hofmann, E. Barnes, and S. Das Sarma, Phys. Rev. B **92**, 115101 (2015).

[39] S. Y. Xu, I. Belopolski, N. Alidoust, M. Neupane, G. Bian, C. Zhang, R. Sankar, G. Chang, Z. Yuan, G. C. Lee *et al.*, Science **349**, 613 (2015).

[40] B. Q. Lv, N. Xu, H. M. Weng, J. Z. Ma, P. Richard, X. C. Huang, L. X. Zhao, G. F. Chen, C. E. Matt, F. Bisti *et al.*, Nat. Phys. **11**, 724 (2015).

[41] L. X. Yang, Z. K. Liu, Y. Sun, H. Peng, H. F. Yang, T. Zhang, B. Zhou, Y. Zhang, Y. F. Guo, M. Rahn *et al.*, Nat. Phys. **11**, 728 (2015).

[42] B. Q. Lv, H. M. Weng, B. B. Fu, X. P. Wang, H. Miao, J. Ma, P. Richard, X. C. Huang, L. X. Zhao, G. F. Chen *et al.*, Phys. Rev. X **5**, 031013 (2015).

[43] X. Huang, L. Zhao, Y. Long, P. Wang, D. Chen, Z. Yang, H. Liang, M. Xue, H. Weng, Z. Fang, X. Dai, and G. Chen, Phys. Rev. X **5**, 031023 (2015).

[44] C. L. Zhang, S. Y. Xu, I. Belopolski, Z. Yuan, Z. Lin, B. Tong, G. Bian, N. Alidoust, C. C. Lee, S. H. Huang *et al.*, Nat. Commun. **7**, 10735 (2016).

[45] Y. Zhou, P. Lu, Y. Du, X. Zhu, G. Zhang, R. Zhang, D. Shao, X. Chen, X. Wang, M. Tian *et al.*, Phys. Rev. Lett. **117**, 146402 (2016).

[46] F. Arnold, M. Naumann, S. C. Wu, Y. Sun, M. Schmidt, H. Borrmann, C. Felser, B. Yan, and E. Hassinger, Phys. Rev. Lett. **117**, 146401 (2016).

[47] B. Xu, Y. M. Dai, L. X. Zhao, K. Wang, R. Yang, W. Zhang, J. Y. Liu, H. Xiao, G. F. Chen, S. A. Trugman *et al.*, Nat. Commun. **8**, 14933 (2017).

[48] C. L. Zhang, Z. Yuan, Q. D. Jiang, B. Tong, C. Zhang, X. C. Xie, and S. Jia, Phys. Rev. B **95**, 085202 (2017).

[49] S. M. Huang, S. Y. Xu, I. Belopolski, C. C. Lee, G. Chang, B. Wang, N. Alidoust, G. Bian, M. Neupane, G. Zhang *et al.*, Nat. Commun. **6**, 7373 (2015).

[50] J. Buckeridge, D. Jevdokimovs, C. R. A. Catlow, and A. A. Sokol, Phys. Rev. B **93**, 125205 (2016).

[51] J. Cardy, *Scaling and Renormalisation in Statistical Physics* (Cambridge University Press, Cambridge, 1996).

[52] T. Meng and L. Balents, Phys. Rev. B **86**, 054504 (2012).

[53] G. Y. Cho, J. H. Bardarson, Y.-M. Lu, and J. E. Moore, Phys. Rev. B **86**, 214514 (2012).

[54] H. Wei, S.-P. Chao, and V. Aji, Phys. Rev. B **89**, 014506 (2014).

[55] P. Hosur, X. Dai, Z. Fang, and X.-L. Qi, Phys. Rev. B **90**, 045130 (2014).

[56] G. Bednik, A. A. Zyuzin, and A. A. Burkov, Phys. Rev. B **92**, 035153 (2015).

[57] Y. Li and F. D. M. Haldane, Phys. Rev. Lett. **120**, 067003 (2018).

[58] E. V. Gorbar, V. A. Miransky, I. A. Shovkovy, and P. O. Sukhachov, J. Phys.: Condens. Matter **31**, 055602 (2019).

[59] D. M. Basko and I. L. Aleiner, Phys. Rev. B **77**, 041409(R) (2008).

[60] S. Murakami, M. Hirayama, R. Okugawa, and T. Miyake, Sci. Adv. **3**, e1602680 (2017).

[61] I. Belopolski, P. Yu, D. S. Sanchez, Y. Ishida, T. R. Chang, S. S. Zhang, S. Y. Xu, H. Zheng, G. Chang, G. Bian *et al.*, Nat. Commun. **8**, 942 (2017).

[62] A. Altland and B. D. Simons, *Condensed Matter Field Theory*, 2nd ed. (Cambridge University Press, Cambridge, UK, 2010).

[63] L. D. Landau and E. M. Lifshitz, *Theory of Elasticity* (Pergamon Press, London, 1959).

[64] D. Chang, Y. Liu, F. Rao, F. Wang, Q. Sun, and Y. Jia, Phys. Chem. Chem. Phys. **18**, 14503 (2016).

[65] D. F. Nelson, *Electric, Optic, and Acoustic Interactions in Dielectrics* (Wiley, New York, 1979).

[66] D. Xue, Y. Zhou, H. Bao, C. Zhou, J. Gao, and X. Ren, J. Appl. Phys. **109**, 054110 (2011).

[67] D. Berlincourt and H. Jaffe, Phys. Rev. **111**, 143 (1958).

[68] M. Acosta, N. Novak, V. Rojas, S. Patel, R. Vaish, J. Koruza, G. A. Rossetti Jr., and J. Rödel, Appl. Phys. Rev. **4**, 041305 (2017).

[69] S.-D. Guo and B.-G. Liu, J. Phys.: Condens. Matter **30**, 105701 (2018).

[70] D. C. Elias, R. V. Gorbachev, A. S. Mayorov, S. V. Morozov, A. A. Zhukov, P. Blake, L. A. Ponomarenko, I. V. Grigorieva, K. S. Novoselov, F. Guinea, and A. K. Geim, Nat. Phys. **7**, 701 (2011).

[71] V. N. Kotov, B. Uchoa, V. M. Pereira, F. Guinea, and A. H. Castro Neto, Rev. Mod. Phys. **84**, 1067 (2012).

[72] B. Roy, J. D. Sau, and S. Das Sarma, Phys. Rev. B **89**, 165119 (2014).

[73] S. Engelsberg and J. R. Schrieffer, Phys. Rev. **131**, 993 (1963).

[74] E. Bauer and M. Sigrist, *Non-Centrosymmetric Superconductors: Introduction and Overview* (Springer-Verlag, Berlin, 2012).

[75] S.-K. Yip, Annu. Rev. Condens. Matter Phys. **5**, 15 (2014).

[76] A. P. Schnyder and S. Ryu, Phys. Rev. B **84**, 060504(R) (2011).

[77] C.-K. Chiu, J. C. Y. Teo, A. P. Schnyder, and S. Ryu, Rev. Mod. Phys. **88**, 035005 (2016).

[78] P. A. Volkov and S. Moroz, Phys. Rev. B **98**, 241107(R) (2018).

[79] Z. Wang and S.-C. Zhang, Phys. Rev. B **87**, 161107(R) (2013).

[80] S. Giraud and R. Egger, Phys. Rev. B **83**, 245322 (2011).

[81] V. Kozii and L. Fu, Phys. Rev. B **98**, 041109(R) (2018).

[82] A. A. Abrikosov and S. D. Beneslavskii, Zh. Eksp. Teor. Fiz. **59**, 1280 (1970) [Sov. Phys. JETP **32**, 699 (1971)].